CHALMERS

Oxidation behavior of selected FeCr alloys in environments relevant for solid oxide electrolysis applications

Master thesis performed at Chalmers High Temperature Corrosion Center

Patrik Alnegren

Department of Chemical and Biological Engineering

Inorganic Environmental Chemistry

CHALMERS UNIVERSITY OF TECHNOLOGY

Gothenburg, 2012

Oxidation behavior of selected FeCr alloys in environments relevant for solid oxide electrolysis applications

Master of Science Thesis in Chemical Engineering
30 credit points

Patrik Alnegren

2012

CHALMERS UNIVERSITY OF TECHNOLOGY

Supervisor: Jan Froitzheim

Examiner: Jan-Erik Svensson

Abstract

If society is to move towards using more renewable energy sources the power fluctuations of e.g. wind and solar energy need to be balanced. Energy storage by production of hydrogen from solid oxide electrolysis cells (SOEC) offers a solution to overcome these obstacles. However, the performance of current SOECs decreases too fast for the technology to be commercialized. This drop in performance over time is partly due to the degradation of metallic interconnects (bipolar plates) within the cell stacks. This study investigates the corrosion performance of selected ferritic steels in simulated SOEC environments. Ferritic steels have many properties that are desirable for interconnects but suffer from oxidation and chromium evaporation over time. Four different FeCr alloys have been exposed in different partial pressures of dry O_2 (anode side) and in 34% H_2O -3% H_2-Ar (cathode side) at 850°C and gravimetrical measurements have been performed to study oxidation rates. Chromium evaporation has been measured and compared for the oxygen containing environments. Chromium evaporation was found to vary largely with oxygen partial pressure, while the oxidation rate of the steels did not vary substantially in the different oxygen partial pressures. Differences in oxidation behavior of the steels were observed between the exposures in different partial pressures of dry O_2 and in 34% H_2O - 3% H_2 -Ar. Both reduced and increased oxidation rates were observed in the steam with hydrogen environment compared to the oxygen environments for different materials.

Keywords: Solid oxide electrolysis cell, SOEC, SOFC, degradation, high temperature corrosion, chromium evaporation, denuder technique

Table of contents

Abstract III
Table of contents IV
1 Introduction 1
1.1. Aim 2
2 Theory 2
2.1 Electrolysis cells 2
2.2 SOC 4
2.3 Corrosion 6
2.3.1 Thermodynamics 6
2.4 Scale formation and growth 8
2.4.2 Kinetics 13
2.5 Chromium evaporation 15
2.6 Interconnect design 16
2.6.1 Ferritic stainless steel interconnects 17
2.6.2 Alloying elements in ferritic stainless steel interconnects 19
2.7 Degradation of SOEC 20
3 Experimental 21
3.1 Material 21
3.2 Exposures 21
3.2.1 Oxygen side exposures (gravimetric) 21
3.2.2 Fuel side exposures (gravimetric) 22
3.2.3 Chromium evaporation 23
3.3 Analysis 24
3.3.1 Calibration of spectrophotometer 24
4 Results 26
4.1 Gravimetrical investigations 26
4.2 Morphology and microstructure 33
4.3 Chromium-evaporation 39
5 Discussion 40
5.1 AL 441 HP 40
5.2 E-brite 41
5.3 Crofer 22H 42
5.4 Sanergy HT 43

5.5 Oxygen pressure dependence 45
5.5.1 Oxidation 45
5.5.2 Chromium evaporation 46
5.6 Estimated steel life time 48
6 Conclusions 49
6.1 Restrictions 50
6.2 Suggestions for future work 50
7 References 50

1 Introduction

Global warming due to increased atmospheric carbon dioxide from fossil fuel combustion is a commonly accepted fact. Adding the diminishing supply of oil and the increasing oil price there are both economic and environmental incentives towards alternative energy sources and energy carriers. One major issue in achieving sustainable energy production is the substantial fluctuation of many renewable energy sources, such as wind, wave and solar power, which makes balancing grid load difficult. To use hydrogen as energy storage and energy carrier offers great possibilities for society to move towards a carbon free economy, but in order to be able to realize a hydrogen infrastructure cheap and efficient hydrogen production is necessary.

Hydrogen is currently almost exclusively produced from hydrocarbons, of which most of them come from fossil fuels [1]. Electrochemical production of hydrogen works by splitting water into hydrogen and oxygen gas. Powered by renewable energy sources, these electrochemical processes offers means of cleaner production of hydrogen compared to traditional fossil fuel reforming. Commercially available electrochemical methods, such as alkaline water electrolysis and proton exchange membranes, operate at temperatures below 100°C. In recent years solid oxide electrolysis cells (SOEC) have gained increased attention. These cells are operated at high temperatures (>600°C) and offer many advantages over conventional electrolysis, such as reduced required electrical power [2] and increased hydrogen production density [3]. Another powerful advantage of SOEC technology is that because of the high operating temperature CO_2 can be electrolyzed to CO[4] and even co-electrolysis of hydrogen to produce syngas [5][6]is possible. This offers the possibility for fossil fuel independent production of hydrocarbons if the electrolysis is powered by e.g. wind power. Most SOECs rely on basically the same technology as solid oxide fuel cells (SOFC), which commonly uses yttria stabilized zirconia (YSZ) as oxygen ion conducting electrolyte. Indeed several studies have included cell stacks operating successfully in both SOEC and SOFC mode [7][8][9][10]. The use of SOEC in combination with SOFC technology offers great potential to balance power fluctuations from renewable energy sources by using hydrogen as energy storage.

The high degree of similarity between SOFC and SOEC technology has enabled SOEC development to achieve substantial success in short time since many technical issues have already been addressed in SOFC related research. The same is true for the choice of interconnect materials for SOEC which relies basically on studies carried out in the SOFC context. The role of the interconnect component in SOEC and SOFC units is to electrically connect individual cells in series to form a multi-cell stack with higher power density. Ferritic stainless steels have many desirable properties for use in solid oxide cell stacks and are the most common type of materials used as interconnect.

Degradation of stack performance over time is an issue that needs to be solved before SOEC can be a competitive technology for commercial electrolysis. Due to the high efficiency of existing water electrolysis technology (and even more so for SOEC) the two main factors that should affect hydrogen cost are electricity price and durability of the electrolyzer system according to a study by John A. Turner [11]. Known degradation phenomena can be partly linked to the degradation of metallic interconnects. Known issues with steel interconnects are increased contact resistance due to oxide scale growth and evaporation of chromium species and consequent poisoning of the cathode in SOFCs [12].

More than a decade of research has led to substantial progress in the development of ferritic steel interconnects for SOFC, but little research has been done to evaluate these interconnects in SOEC applications. It is expected that due to the high degree of optimization achieved in SOFC steel development a change in environment leads to different priorities regarding materials optimization. Hence this study focuses on degradation phenomena of ferritic steel interconnects in SOEC relevant environments, where the major difference lies on the oxygen side where the oxygen partial pressure is higher and the atmosphere drier for SOEC.

1.1. Aim

The aim of this thesis is to test the degradation performance of different commercial steels under simulated SOEC environments. The work is focused on oxidation behavior and evaporation of volatile chromium species, both phenomena closely linked to cell stack degradation. The aim is not to do in-depth studies of oxidation mechanisms, but to do a more widespread research in the relatively new field that is SOEC. By doing this, the hope is to discover which the differences and similarities between the degradation behavior of ferritic steels in electrolysis environments compared to fuel cell environments are, to see what can be linked to knowledge achieved in the more studied field of SOFC. Future commercial SOEC stacks may be run at pressures well above atmospheric, which could lead to faster degradation of ferritic steel interconnects. Hence, this study will have substantial focus on finding correlations between degradation behavior and oxygen partial pressure.

2 Theory

2.1 Electrolysis cells

In chemistry, electrolysis is the process of driving a nonspontaneous chemical reaction by using applied direct current [13], thus converting electrical energy into chemical energy. Just as with galvanic reactions the resulting voltage potential needed to drive an electrolysis reaction can be derived from the Nernst equation (2.1) and standard potentials from the electrochemical series.

$$E = E° - \frac{RT}{nF} lnQ \qquad (1)$$

where E is the cell potential, E° the standard cell potential, R the gas constant, T the temperature, n the stoichiometric coefficient of transferred electrons, F the Faraday's constant and Q the reaction quotient for the cell reaction. Electrolysis reactions differ from spontaneous galvanic reactions in that an external electric power source is needed to drive the reaction [13]. Equation (1) gives the theoretic thermodynamic value for the required potential to drive a reaction, however in reality a larger potential is needed. The additional potential is called overpotential which is due to electrochemical kinetics at the electrode surface. The overpotential is needed to overcome activation energy barriers for electron transfer in the half-cell reactions at the anode and cathode interfaces [14] and is affected by e.g. type of electrodes and temperature. The reaction chamber in which electrolysis reaction takes place is called an electrolysis cell and normally consists of two electrodes (anode and cathode), electrolyte and external wiring coupled to an electric power source (see Figure 1). Oxidation takes place at the anode and reduction at the cathode and the ions produced by the half-cell reactions on the electrodes are transported through the electrolyte.

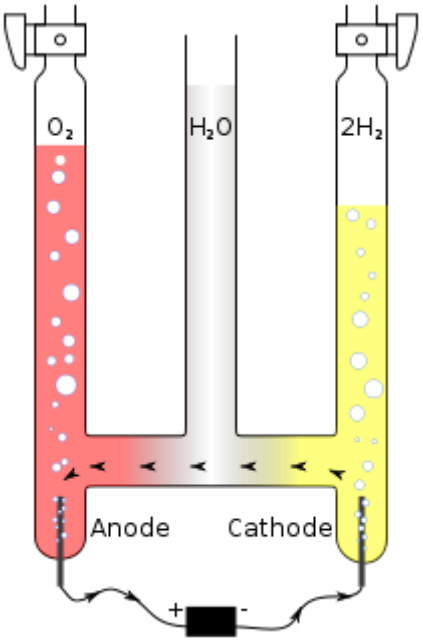

Figure 1. A schematic illustration of a so called Hoffman cell [15]. This is a type of electrolysis cell that is can be used for electrolyzing water into hydrogen and oxygen gas.

Hydrogen is a most promising future energy carrier and can be produced by simple electrolysis of water. The theoretical potential required to drive water electrolysis under standard conditions (1 atm, 25°C) is 1.23V, but in reality a quite substantial overpotential is needed. There are several types of electrolysis cell technologies available, operating at different temperatures and pressures. In the low temperature range alkaline water electrolysis and permeable electrolyte membrane (PEM) electrolysis cells are two common and well established techniques [2]. Solid oxide electrolysis cells (SOEC) operate at temperatures of 600°C and above and are often referred to as high temperature steam electrolysers (HTE).

The theoretical potential, or Nernst potential, needed for an electrolysis reaction is a function of temperature. The total energy demand (or gain) for a chemical reaction is given by (2)

$$\Delta H = \Delta G + T\Delta S \tag{2}$$

where H is the enthalpy, G is Gibbs energy and S is entropy. Gibbs energy is related to electrical energy, or cell potential, by (3), which is the relation that allows for deriving the Nernst equation (1). [16]

$$\Delta G = -nFE \tag{3}$$

This means that at higher temperatures the electrical energy requirement is diminished so that cells which operate at higher temperatures need less applied voltage for the electrolysis reaction to proceed. In Figure 2 heat, electrical and reaction enthalpy for water electrolysis are plotted against temperature. The total reaction enthalpy ΔH increases with temperature, but only slightly compared to the drop in electrical energy. An additional factor that is affected by temperature is overpotential. As the temperature increases the overpotential decreases, thus reducing the needed cell potential further at higher temperatures [2]. The overall cell voltage can be approximated as the sum of the Nernst potential for the reaction, the overpotential and

the ohmic resistance over the cell [17]. The theoretical cell potential for an electrolysis reaction will be converted into chemical energy, but the inevitable additional electrical energy will be converted into heat. Cells that operate at higher temperatures will use this generated heat for the splitting of water, thus utilizing more of the input energy and increasing the efficiency. A term commonly used in electrolysis contexts is the thermoneutral potential. This basically means the potential at which the generated heat is equal to the heat consumed by the electrolysis reaction [2]. When operating below the thermoneutral potential heat needs to be supplied (endothermic operation) and when operating above heat needs to be removed, or cooled off, in order to maintain the desired working temperature (exothermic operation). Assuming that there are no short-circuits in a cell the production rate of hydrogen will have a linear dependency on the electrical current through the cell [13]. The electrical current can, according to Ohm's law, be adjusted by the applied potential.

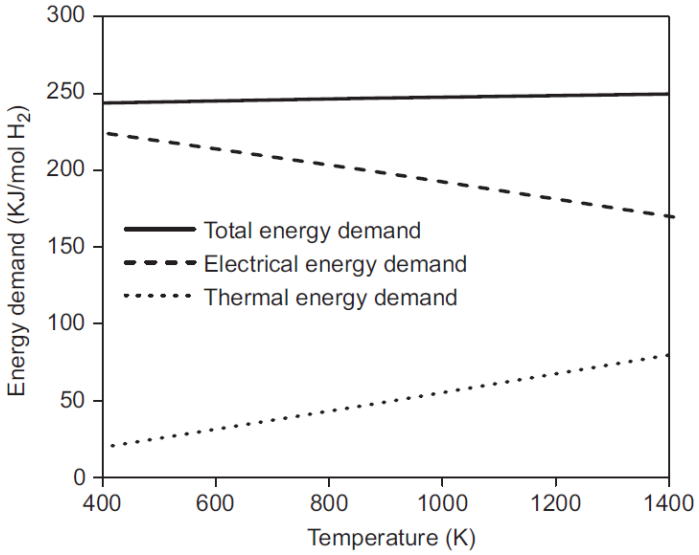

Figure 2. Calculated total energy demand ΔH, electrical energy demand ΔG and thermal energy demand TΔS for steam electrolysis are plotted against temperature [18].

2.2 SOC

Solid oxide cells (SOC) can be used to electrolyze steam into hydrogen and oxygen (SOEC mode). This reaction requires input of electrical energy e.g. from wind turbines or nuclear power plants. SOC can also be used reversibly as solid oxide fuel cells (SOFC mode), harnessing the reaction energy from hydrogen being oxidized to water and converting it to electrical energy [2]. In fact current SOEC technology has been able to progress rapidly by benefiting on development of SOC for fuel cell operation.

Solid oxide refers to the ion conducting electrolyte material which is a solid ceramic material, commonly made of yttria stabilized zirconia, or in short YSZ. Temperatures of 600-1000°C are needed in order to increase the diffusivity and overcome activation energy in the ceramic electrolyte material and achieve sufficient conductivity for oxygen ions [19]. A schematic picture of a two cell SOEC electrolyzing steam is presented in Figure 3. Vaporized water is fed into the cathode electrode where it gets dissociated into hydrogen and oxygen ions. The hydrogen gas is collected at the cathode outlet, but needs to be separated from residual steam. The applied potential over the cell drives the transport of oxygen ions through the electrolyte.

At the anode electrolyte interface the oxygen ions are oxidized to oxygen gas which is passed through the anode outlet, which can be assisted by using air as a sweeping gas. The electrochemical reactions where the electron transfer occurs are believed to take place at the gas- electrode-electrolyte interfaces. These junctions, where the electrodes meet the electrolyte, are called triple phase boundaries [2][18].

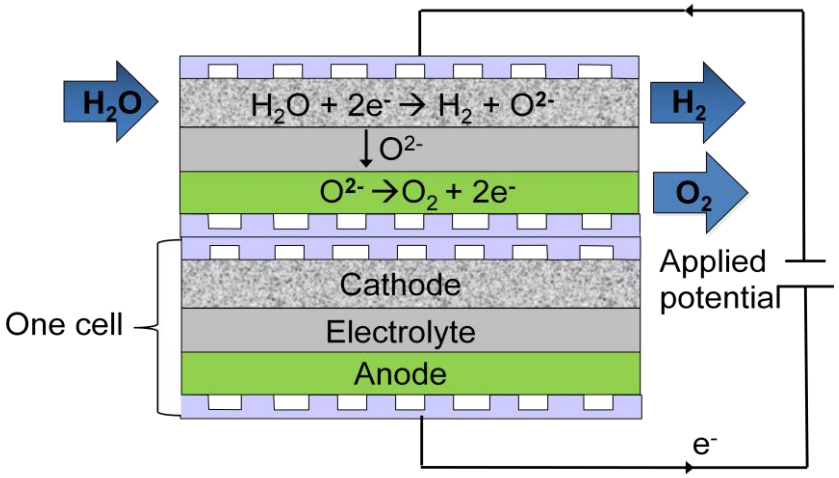

Figure 3. Schematic picture of two solid oxide electrolysis cells coupled in series. The same reactions are occurring in both cells. An applied potential drives the splitting of water molecules into hydrogen and oxygen.

In order to get more power density SOC are coupled in series to form cell stacks. There are two main types of designs for SOC units: tubular and planar stacks. The latter is the design presented in Figure 3, with the electrolyte sandwiched between the electrodes and corrugated interconnects that allows for gas to flow to the electrodes. Tubular SOC usually have their cell components, i.e. anode, cathode and electrolyte, deposited onto a porous ceramic support tube which is permeable to gas [19]. The anode and cathode gases flow through each side of the tube diameter. This report will focus on the planar design where interconnecting plates are used. Planar cell stacks as compared to tubular stacks offers advantages of cheaper production and higher power density and is nowadays the stack design most commonly used for both SOFC and SOEC [2][20][19].

In planar design SOC stacks, the cells are separated by electronically conducting interconnecting plates. These interconnects distribute the current to the cells and separate cathode and anode gases from each other. The gas tightness of the interconnect is crucial since the products of the electrodes would otherwise react with each other to form water again, thus rendering the electrolysis useless. High electronic conductivity is necessary to keep the ohmic losses over the stack low and to keep the efficiency of the stack high. The material choices for the interconnects in SOC are perovskite-type ceramics based on rare earth chromites, such as lanthanum chromite, or metallic alloys [19]. As development of SOC has lead to decreased operating temperatures metallic interconnects have become more common. More information regarding interconnects will be provided in section 2.6.

The cathode, where the fuel or hydrogen is generated, is most commonly made up of a porous mix of metallic nickel and electrolyte material (commonly YSZ) [2]. The mix ensures good

adhesion to the electrolyte and matching of thermal expansion coefficient [19]. Nickel is chosen due its catalytic properties and is especially important when SOFC stacks are fed with syngas since it catalyses the reformation of methane into hydrogen and carbon monoxide. The oxygen electrode, or anode, is normally made up of a lanthanum strontium manganite (LSM) and YSZ composite [2]. The electrodes should have high catalytic properties to increase the reaction kinetics and thus lowering the polarization resistance of the cell.

The change in volume of solids with temperature can be compared by their coefficient of thermal expansion (CTE). It is crucial for a planar cell stack to have reasonably matching CTE's of all its components: electrodes, electrolyte and interconnects. If this is not the case, cracks due to internal stresses will occur during thermal cycling of the stack (turning on and off). This is part of the reason why electrolyte material is commonly mixed in with electrode material. By doing this an electrode-electrolyte gradient is created which increases the tolerance to thermal cycling due to the resulting gradient of thermal expansion properties.

2.3 Corrosion

Corrosion is the process of deterioration of a material. Corrosion of metals is most commonly deterioration of caused by reaction of the metal and oxygen which causes the metal to be gradually transformed into metal oxide. All metals except precious metals like gold oxidize under ambient conditions and will eventually go back to a form similar to or to the ores they were originally refined from. The reason why many metals seem to be unaffected under normal dry conditions is that they form thin invisible layers of metal oxide on the surface that protects the base metal from oxygen exposure. However, by diffusion of metal or oxygen ions through this layer oxidation is still occurring, though at a negligible pace. When the temperature is increased well over ambient temperatures reaction rates speed up by an Arrhenius correlation and corrosion becomes a problem again. At higher temperatures other problems, such as volatilization or melting of the protective oxide layer or cracking due to induced stresses in the material might occur. The following section will briefly go through the fundamentals of high temperature corrosion of metals.

2.3.1 Thermodynamics

The second law of thermodynamics tells us whether a chemical reaction is possible or not. At constant pressure and a certain temperature Gibb's free energy (4) can be used to determine if a reaction is spontaneous or not. Here equation 2 is rewritten as:

$$\Delta G = \Delta H - T\Delta S \tag{4}$$

If $\Delta G = 0$ the reaction is in equilibrium, $\Delta G > 0$ the reaction is non-spontaneous and if $\Delta G <$ the reaction is spontaneous.

A chemical reaction, e.g. the oxidation of metal can be described in terms of Gibb's free energy. If the following reaction is considered:

$$xM + \frac{y}{2}O_2 \leftrightarrow M_xO_y \tag{5}$$

where M represents an arbitrary metal, this can be described as:

$$\Delta G = \Delta G° + RTln\left(\frac{a(M_xO_y)}{a(M)^x a(O_2)^{\frac{y}{2}}}\right) \quad (6)$$

Where ΔG° is the free energy change when all species are in their standard states, R is the ideal gas constant and a is the thermodynamic activity of a specific species. The activity of pure solids, in this case the metal and its oxide, can be approximated as unity. When the reaction is in equilibrium ΔG is equal to zero and the equation can then be written as

$$\Delta G° = -RTln\left(\frac{1}{a(O_2)^{\frac{y}{2}}}\right) \quad (7)$$

and if the oxygen activity is approximated as oxygen partial pressure this becomes

$$p_{O_2} = exp\left(\frac{\Delta G°}{RT}\frac{2}{y}\right) \quad (8)$$

This equation allows one to calculate if a metal or oxide is thermodynamically stable or not at a certain temperature and oxygen partial pressure. The oxygen pressure where metal and oxide are in equilibrium is called dissociation pressure. At a oxygen partial pressure below the dissociation pressure the oxide is reduced to metal and above the dissociation pressure the metal is oxidized. Ellingham and Richardson constructed a diagram representing this correlation (see Figure 4). In this diagram standard free energy of formation is plotted versus temperature and dissociation pressure and there are guiding points and surrounding axes representing oxygen partial pressure that allows for quick calculation of the dissociation pressure by drawing lines from the guiding points through the temperature – metal intersection for a specific metal. The Ellingham/Richardson diagram can also be used for comparison between the stability of different metals and oxides. The lower the line is in the diagram the more stable is the oxide and consequently a metal is more stable the higher its line is in the diagram. [21]

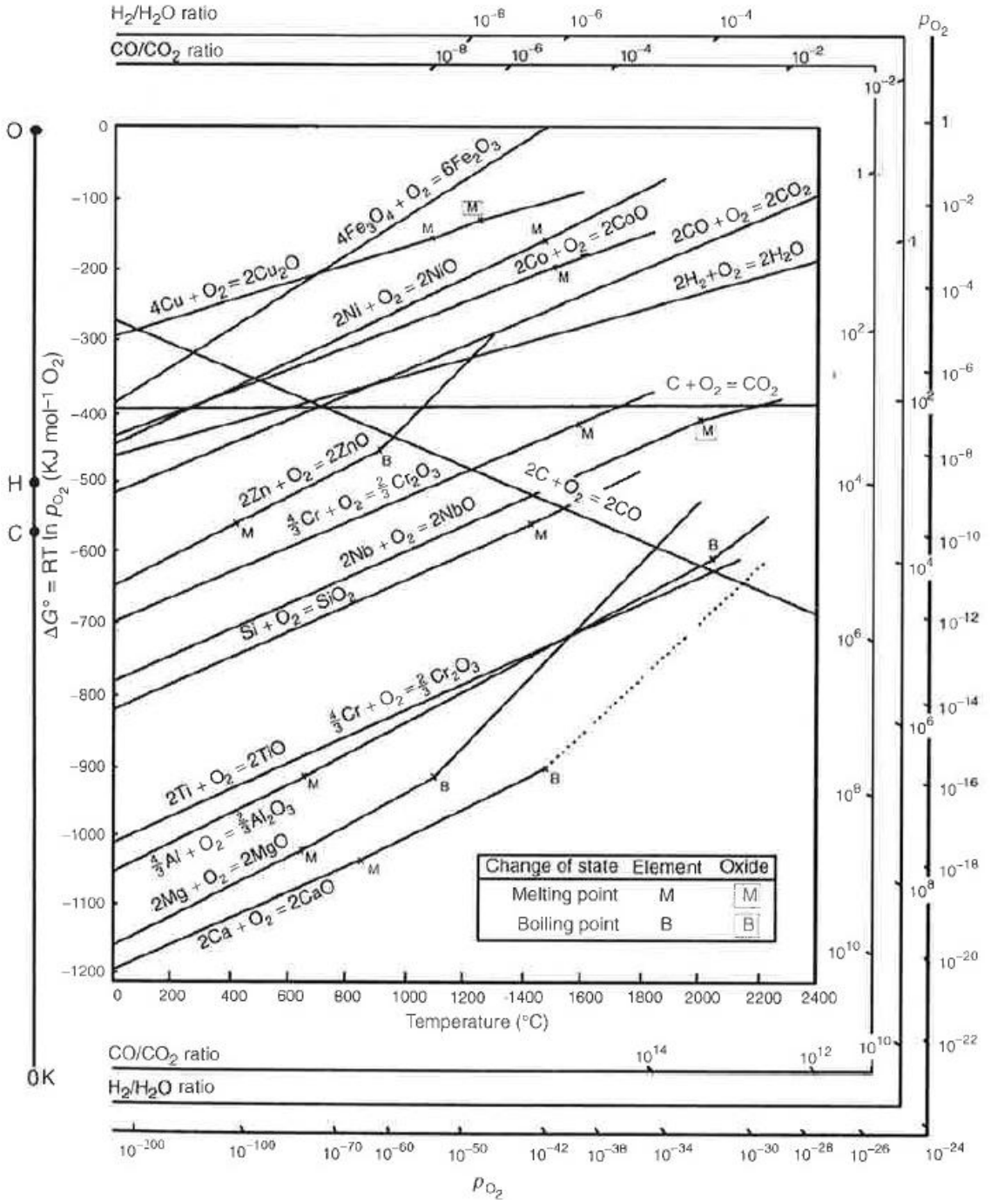

Figure 4. Ellingham/Richardson diagram. Standard free energy of formation for selected oxides are plotted against temperature [21].

2.4 Scale formation and growth

On an ideal clean metal surface oxidation occurs in three stages:

- adsorption of oxygen gas on the surface
- formation of oxide nuclei and lateral growth of these nuclei until a continuous oxide film is formed
- growth of the oxide film perpendicular to the metal surface.

This is schematically illustrated in Figure 5. At atmospheric conditions the two first stages happen in an instant and can only be observed at lower oxygen partial pressures. Once a continuous oxide film is formed the oxidation proceeds by thickening of this film. At this stage the mechanism is completely changed. Oxygen and metal are now separated by an oxide film and all further reaction has to be preceded by solid state diffusion through the oxide film. Diffusion can be either metal cation diffusion, oxygen anion diffusion or both. At atmospheric pressures the diffusion through the oxide scale is often the rate determining step for the oxidation process which leads to reduction of the oxidation rate as the scale grows thicker. It should be noted however that not all metals form dense oxide layers but might instead have porous oxide structures which allows gas transport through the scale and thus offer less protection against continued oxidation. Oxide structures can be crystalline, amorphous or vitreous. The latter is a non-crystalline structure just like for amorphous materials but it possesses short range order, but no long range order. An example of a vitreous oxide film is SiO_2, which is one of the few oxides that keeps its non-crystalline form at higher temperatures. Films of Cr_2O_3 are vitreous at room temperature but become crystalline at higher temperatures. Since the scale is initially formed by many oxide nuclei it will consist of multiple crystals and thus be polycrystalline. Polycrystalline films have incoherent boundaries between the oxide nuclei, called grain boundaries. These grain boundaries may provide paths of easier diffusion through the oxide film.[22]

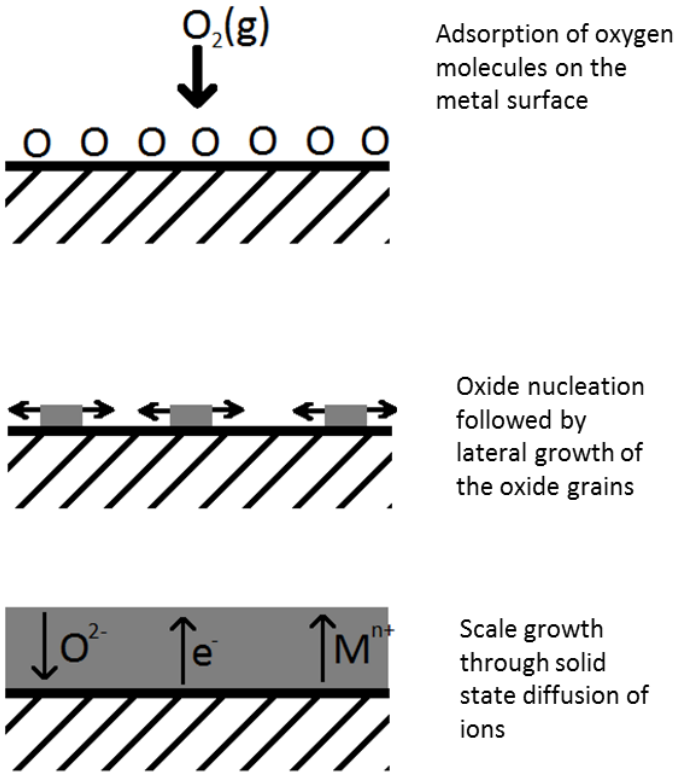

Figure 5. Schematic illustration of the initial stages of oxidation of a clean metal surface. From the top: adsorption of oxygen gas, oxide nucleation and lateral growth followed by increased thickness of the oxide layer by ion diffusion.

The direction in which oxide scale is growing is determined by the type of ion diffusion through the scale. If the diffusion is predominated by oxygen ion diffusion the oxide scale will grow

inwards towards the metal or if metal ion transport is predominant the scale growth will proceed outwards. Figure 6 depicts a simplified model of how metal oxide is formed either at the metal/scale interface in case of anion mobility or at the oxide/gas interface in the case of cation mobility. To understand why anion or cation transport could be predominant one must look at the types of defects in oxide crystals. The oxide crystals are ordered arrays of metal cations and oxygen anions. However, due to entropic forces crystals have defects of different types depending on the properties of the elements which they are made up of. The defect structure depends on temperature, oxygen partial pressure and the energy of formation for a specific defect in a lattice. The type of defect governs which type of diffusion mechanism will be predominant. Like semiconductors, oxides are classified into n- or p-type depending how electrical charge is transported. N-type oxides carry electrical charges by electrons in the conduction band and p-type oxides by electron holes in the valence band [21][23].

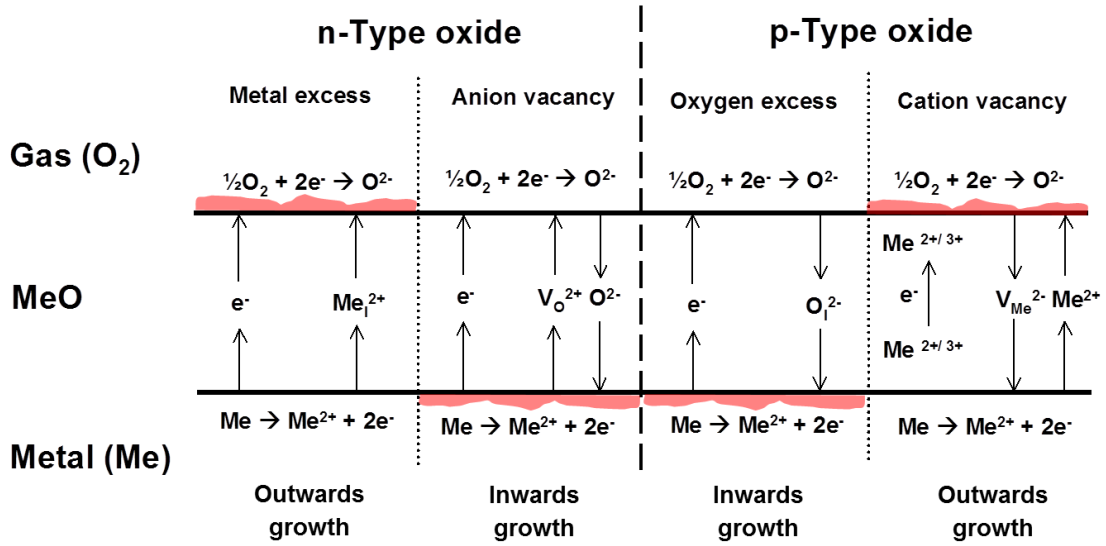

Figure 6. Simplified model of diffusion controlled oxidation. If the oxide is predominated by oxygen vacancies or oxygen excess the oxidation will take place at the metal/oxide interface. Metal excess or vacancy results in oxide growth at the oxide/gas interface.

N-type oxide semiconductors are divided into two groups, i.e. excess metal or oxygen deficient but can also be a combination of both. Metal excess oxides have interstitial cations in the lattice that are compensated for by equal charge of electrons in the conduction band. Cations can thus be conducted through the lattice by changing interstitial sites. N-type oxides can also have oxygen vacancies which results in positive charges that also are compensated for by conduction band electrons. By the same reasoning, p-type oxides are metal defiant or have excess oxygen resulting in negative charges that are compensated for by electron holes in the valence band. Excess ions, i.e. interstitial ions, can diffuse through the oxide by changing interstitial sites. Ion vacancies can also diffuse in the lattice resulting in conduction of the vacant ion species. The effect on scale growth depending on the type of predominant defect in the oxide is summarized in Figure 6 [21][22].

In order for an oxide film to offer good protection against corrosion it needs to be dense and cover the metal surface. Looking at scale growth at a larger length scale there are a number of mechanisms that can lead to stresses in the oxide or metal that causes the scale to crack or spall

of. A general rule is that the thicker an oxide layer is the larger are the stresses acting on it and the more likely it is to break. Below follows some mechanisms that induces stress during oxide scale growth.

2.4.1.1 Pilling- Bedworth ratio

Metals and their corresponding oxides seldom have the same specific volume. When oxidation occurs by inwards growth the volume mismatch between oxide and metal results in induced growth stresses. In 1923 Pilling and Bedworth proposed a method for classifying the growth stresses on metals and oxides with known oxide to metal volume ratios [24]. The ratio of the volume of the oxide divided by the volume of the metal is called the Pilling Bedworth ratio (PBR). Oxide-metal volume ratios are listed in Figure 7. If PBR is above 1 the growth stress are compressive and the oxide will initially be protective. If PBR is below 1 the growth stresses are tensile and the oxide will fail to cover the metal surface. However, the latter statement has been proven not to be true for thin film formation on alkali and alkaline earth metals but true when the oxides grew thicker. The PBR can thus be used as tool for anticipating oxide growth behavior but is only one of many factors that affect oxide growth stresses. Furthermore, when oxidation proceeds by outwards growth the concept of PBR becomes invalid since the oxide is not constrained to occupy the consumed metal [21][22].

Oxide	Oxide–metal-volume ratio
K_2O	0.45
MgO	0.81
Na_2O	0.97
Al_2O_3	1.28
ThO_2	1.30
ZrO_2	1.56
Cu_2O	1.64
NiO	1.65
FeO (on α-Fe)	1.68
TiO_2	1.70–1.78
CoO	1.86
Cr_2O_3	2.07
Fe_3O_4 (on α-Fe)	2.10
Fe_2O_3 (on α-Fe)	2.14
Ta_2O_5	2.50
Nb_2O_5	2.68
V_2O_5	3.19
WO_3	3.30

Figure 7. PBR ratios of some common metals [21].

2.4.1.2 Epitaxial stresses

When oxide nucleates starts to form on a metal surface they will grow with a preferred orientation with respect to the substrate surface which is referred to as epitaxial growth. Due to differences in metal and oxide lattice parameters this may lead to induced stresses as the oxide growth proceeds. The stresses will be largest at the metal oxide interface.

Oxidation rate can be dependent on the grain orientation on a surface. Different oxidation rates of neighboring grains and faster diffusion rate and oxide formation along grain boundaries may lead to stresses being developed at grain boundaries.

2.4.1.3 Compositional changes in the alloy or scale

When alloys are oxidized one element is usually preferentially oxidized which may lead to depletion of this element and a local change in the alloy composition. Compositional changes in the alloy may lead to changes in the lattice parameters which may lead to stresses. Likewise, compositional changes in the oxide may also result in stresses.

2.4.1.4 Stresses induced by certain growth mechanisms

When cation transport is predominant voids and cavities may form at the metal/scale interface since metal is being transported to the oxide surface. Thin oxide films may initially deform and keep contact with the metal, but as the film grows thicker more force is required to deform it and voids and cavities are formed. When the oxide film continues to grow stresses build up between oxide and metal. When oxidation occurs by a mix of cation and anion diffusion oxides may form within the oxide scale which will result in growth by thickening of the scale and by lateral growth. Such growth induces larger stresses and may lead to cracking of the oxide film.

2.4.1.5 Thermal stresses

Thermal stresses are common causes to cracking and spalling of oxide scales but is not related to the oxide growth mechanism. When a metal-oxide system is cooled down stresses may be induced due to differences in coefficients of thermal expansion (CTE) between oxide and metal. Figure 8 shows a list of CTEs for some metals and corresponding oxides. Scales of Cu_2O may spall violently when cooled to room temperature quickly due to the large mismatch of CTE between Cu_2O and Cu. If the scale can tolerate thermal cycling or not does not solely depend on the ratio of metal and oxide CTEs, but also on factors like scale adherence to the metal and thickness of the scale.

Linear Thermal Expansion Coefficients of some Metal/Oxide Systems[29]

System	*Oxide coefficient* $\times 10^{-6}$	*Temperature range (°C)*	*Metal coefficient* $\times 10^{-6}$	*Temperature range (°C)*	*Ratio*
Fe/FeO	12·2	100–1000	15·3	0–900	1·25
Fe/Fe_2O_3	14·9	20–900	15·3	0–900	1·03
Ni/NiO	17·1	20–1000	17·6	0–1000	1·03
Co/CoO	15·0	20–900	14·0	0–350	0·93
Cr/Cr_2O_3	7·3	100–1000	9·5	0–1000	1·30
Cu/Cu_2O	4·3	20–750	18·6	0–800	4·32

Figure 8. CTEs of some common metals and oxides are listed [22].

2.4.1.6 Response to stresses

The most severe responses to growth and thermal stresses are cracking and spalling of the oxide since this leaves the metal beneath unprotected against further oxidation. Growth stresses may also result in buckling of the oxide scale or of the alloy. Tension in the oxide leads to crack formation. Compression of the oxide scale is the more common scenario for engineering alloys due to both compressive growth stresses and compression during cooling because of CTE mismatches. Figure 9 schematically depicts metal-oxide responses to compressive stress. Compressive stresses can cause oxide scales to spall and the tendency increases with: increasing stress force, increasing scale thickness and decreased adhesion [21][22].

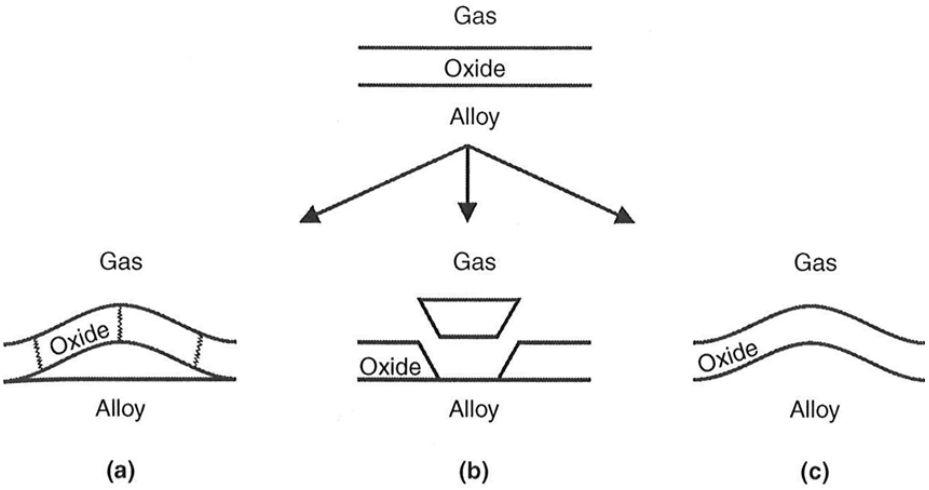

Figure 9. Examples of responses of oxide scales to compressional stress. (a) Buckling of the oxide, (b) shear cracking of the oxide, (c) plastic deformation of the oxide and alloy [21].

2.4.2 Kinetics

From Figure 4 it is evident that the thermodynamic stability of metals is increasing with increased temperature. This might seem contradictory since corrosion of metals in most cases is accelerated at higher temperatures. From an entropic perspective the increased stability might seem more intuitive since solid metal and gaseous oxygen, two species, are combined to one solid oxide species and thus more order is created. This decrease in entropy results in larger energy losses at higher temperatures and thus the driving force for the reaction decreases with increased temperature. The reason for the accelerated corrosion rate has to do with reaction kinetics.

There are many factors which determine the oxidation rate such as temperature, oxygen pressure, metal pretreatment and elapsed time of oxidation. By measuring the mass gain of a metal or alloy over time one can study the oxidation kinetics in a certain environment, assuming that the oxide is well adherent to the metal and does not spall off. Oxidation rates are typically classified to fit linear, logarithmic or parabolic rate equations. Classifying the oxidation rate to a rate equation is not sufficient to determine the oxidation mechanism, but it can help in predicting the continued oxidation rate and can often limit the interpretation to a group of mechanisms. Oxidation rates need not fit any of the rate equations mentioned above or a combination them by changing mechanism as the oxidation proceeds [21][22].

2.4.2.1 Linear rate equation

When oxidation rate is limited by interface reactions and more often the oxide/gas interface oxidation proceeds at constant rate can be fitted to a linear rate equation:

$$x = k_1 t \tag{9}$$

Where x is the thickness of the oxide film, k_1 the rate constant and t elapsed exposure time. Linear oxidation rates are often observed when the oxide film is very thin and solid state diffusion is not the rate limiting step which is the case in the beginning of many oxidation processes. Linear oxidation can also be observed if the oxide film is destroyed by e.g. spalling off and this is often referred to as break away corrosion.[22]

2.4.2.2 Parabolic rate equation

When oxidation rate is controlled by diffusion through the oxide scale it can often be fitted to a parabolic rate equation. This is often the case for many metals oxidized at high temperatures. In 1933 Wagner proposed a model for oxidations at high temperatures based on a number of assumptions. The most important assumptions where rate limiting diffusion through the scale and steady state conditions of oxygen partial pressures at the metal/oxide and oxide/gas interface. Ion flux through a medium under such conditions can be described by Fick's first law of diffusion (10). The ion flux (j) is proportional to the chemical potential (Δμ) over the scale with thickness (x).

$$j = -D\frac{\Delta\mu}{x} \tag{10}$$

Furthermore, scale growth rate can be described as the product of ion flux times the molar volume (V_{ox}) of the formed oxide.

$$\frac{dx}{dt} = j * V_{ox} \tag{11}$$

If K_p substitutes the product of the chemical potential, diffusion coefficient and molar volume and the expression is integrated it yields to the common parabolic growth rate equation [25][22]:

$$x^2 = 2K_p t \tag{12}$$

2.4.2.3 Logarithmic rate equation

It is common for many metals at temperatures below 300-400°C to have oxidation rates that can be fitted to logarithmic rate equations, i.e. initially rapid oxidation that decreases significantly to negligible rates with time. Logarithmic oxidation rate equations include direct logarithm and inverse logarithm respectively:

$$x = k_{log}\log(t + t_0) + A \tag{13}$$

$$\frac{1}{x} = B - k_{il}\log t \tag{14}$$

Where A and B are constants and k_{log} and k_{il} rate constants [22].

2.4.2.4 Factors affecting the rate constant

As with all chemical reactions there are activation energies related to the oxidation of metals. An Arrhenius relationship between reaction rate constant and temperature can thus be assumed and rate constants can be described by:

$$k = k_0 \exp\left(-\frac{Q}{RT}\right) \tag{15}$$

where Q is the activation energy. In Wagner's theory of parabolic oxidation the rate constant in this expression can be related to the self-diffusion coefficient of the ions in the oxide. Depending on the conditions and type of oxides, the oxygen partial pressure may also affect the rate constant of oxidation. At very low oxygen partial pressures, when adsorption is rate

limiting, the rate of reaction is proportional to the oxygen partial pressure and under linear phase boundary controlled oxidations it is proportional to square root of oxygen partial pressure. Even when the oxidation rate is diffusion controlled the reaction rate can depend on oxygen partial pressure. If the oxide is non- stoichiometric and is metal deficient or has excess oxygen the parabolic rate constant is proportional to $p(O_2)^{1/n}$, where n is a function of the oxide defect structure. Stoichiometric oxides like Cr_2O_3 and Al_2O_3 have fewer defects and thus lower diffusion rates than non-stoichiometric oxides like FeO and Fe_2O_3. Diffusion rate is also affected by the presence of grain boundaries and lattice dislocations that offer alternative diffusion paths compared to lattice diffusion. This type of diffusion is called short-circuit diffusion and usually requires lower activation energy than lattice diffusion. Hence, this is often the predominant diffusion mechanism at lower temperatures and as the temperature increases lattice diffusion becomes a larger part of the total ion flux through the oxide scale. Higher rate constants have been observed in more fine grain oxide films due to the high amount of grain boundary diffusion paths. This also allows short-circuit diffusion to be predominant at higher temperatures [21][22].

2.5 Chromium evaporation

A major issue with chromia forming alloys is the evaporation of hexavalent chromium species at elevated temperatures. This affects the oxidation kinetics of the alloy since volatilization leads to mass transfer of the protective scale away from the substrate. At prolonged oxidation the oxidation rate can change from parabolic to linear due to equilibrium between mass gain from oxidation and mass loss from evaporation. Since chromium is evaporated away the substrate will eventually suffer from chromium depletion. Chromium evaporation also have detrimental effects on cell stacks which will be discussed in section 2.7. Furthermore, hexavalent chromium is cancerogenic, so there are incentives both from a materials and health perspective to reduce the evaporation of chromium from metallic interconnects.

The main volatile species formed from evaporation of Cr_2O_3 in atmospheres containing O_2 and H_2O are CrO_3, $CrO_2(OH)_2$ and $CrO_2(OH)$ [26]. These species are formed by the following reactions:

$$½\ Cr_2O_3(s) + ¾\ O_2(g) = CrO_3(g) \quad (16)$$

$$½\ Cr_2O_3(s) + ¾\ O_2(g) + H_2O(g) = CrO_2(OH)_2(g) \quad (17)$$

Experimental and theoretical studies by Ebbinghaus showed that $CrO_2(OH)_2$ is the major volatile species formed in atmospheres containing water vapour and oxygen [27]. This was also confirmed by extensive experimental studies by Opila who also provided corrections to existing thermodynamical data for formation of $CrO_2(OH)_2$ [26]. As can be seen from (16) and (17) the partial pressure of volatile chromium species is dependent on oxygen and water vapour partial pressure. Experimental values of $CrO_2(OH)_2$ partial pressure are plotted against partial pressure of oxygen and water vapour in Figure 10. Maximum chromium evaporation occurs at roughly equal pressures of H_2O and O_2 [27]. Atmospheric air is normally moist to some extent which leads to predominant formation of $CrO_2(OH)_2$. At very low water vapour pressures, such as at the oxygen side of SOEC units, the partial pressure of chromium reduces significantly and CrO_3 will be the predominant volatile chromium species.

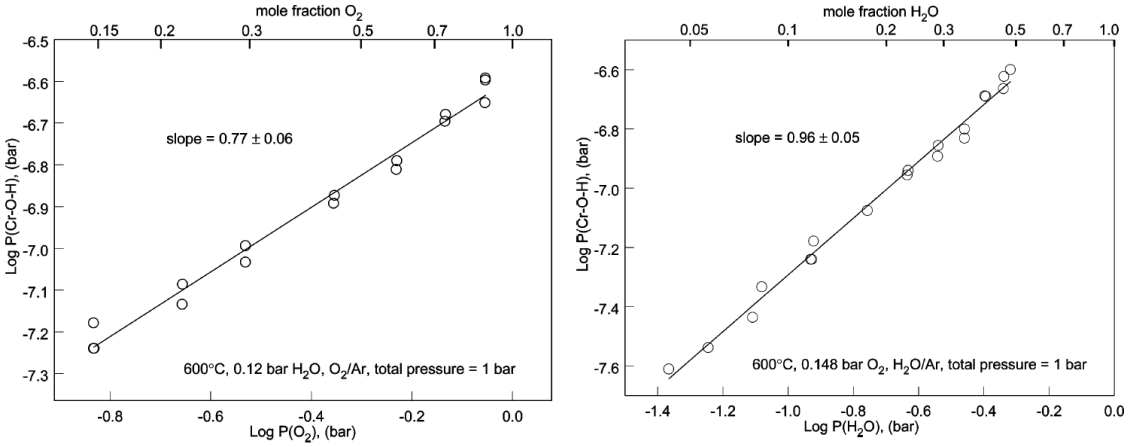

Figure 10. Experimentally achieved values of P($CrO_2(OH)_2$) plotted against P(O_2) (right) and P(H_2O) (left) [26].

The partial pressure of gaseous chromium species has an Arrhenius relationship with temperature, thus reducing the temperature greatly reduces the problems associated with chromium evaporation. What one also has to have in mind when it comes to evaporation rate is the flow profile over the exposed surface. If equilibrium partial pressure of volatile chromium species is reached the evaporation rate will have a linear dependence on flow rate. However, at higher flow rates the chromium evaporation rate is limited by reaction kinetics and becomes independent of flow rate.

2.6 Interconnect design

Interconnects link together repeating solid oxide cells and forms cell stacks by distributing electrical current and separating anode and cathode gases. These cell stacks are operated at temperatures up to 900°C and thus its components must be designed to perform well and be durable at high temperatures. Listed below are the main requirements of interconnects in high temperature SOC stacks [19]:

- High electronic and thermal conductivity and low ionic conductivity of the substrate throughout the stack life time.
- Chemical stability in oxygen and fuel gases and towards other cell components at high temperatures.
- Matching coefficient of thermal expansion (CTE) with the other cell components.
- Impermeability towards gases.
- Sufficient mechanical strength.

There are both ceramic and metallic materials that to some extent fulfill these criteria. Lanthanum chromite ceramics have most of the desired properties listed above and have been used as interconnect material. The cost of these ceramics is however rather high and the material cannot be processed once it is sintered. Other disadvantages with La-chromite interconnects are relatively low thermal conductivity and mechanical strength [19, 28], which makes them less suitable for planar stack design. Metallic interconnects are generally cheaper (except for noble metals), easier to fabricate and are less brittle compared to ceramics.

High temperature alloys generally rely on the formation of a passivating oxide layer that retards the oxidation of the metal surface, thus protecting against further corrosion. Alloys containing Cr, Si or Al are commonly used for high temperature applications as they can form good protective oxide layers of Cr_2O_3, SiO_2 and Al_2O_3 respectively. However, silica and alumina forming alloys are not suitable as interconnect materials as these oxides have too low electronic conductivity which would lead to too large reduction in stack performance due to ohmic losses [28, 29]. Thus when designing alloys for interconnects it is important to keep the Si and Al concentrations low to avoid the formation of continuous silica or alumina layers.

Chromia has several orders of magnitude higher electrical conductivity than silica and alumina and is therefore the preferred passivating layer former for metallic interconnects. The downside of Cr_2O_3 is that it has, compared to SiO_2 and Al_2O_3, a higher growth rate and can therefore not be used at as high temperatures as La-chromites. Austenitic chromia forming steels are Fe-Cr alloys that adopts the FCC structure due to the mix in with an austenitic stabilizer, such as Ni [22]. These steels have 18-30wt% chromium and have good corrosion resistance at high temperatures, but their thermal expansion coefficient is too large compared to other cell components in SOCs and are therefore not very suitable as interconnect materials [30, 31]. They could possibly be used at lower temperatures of around 600°C where materials can be made thinner and CTE is not as large issue [32]. Among the Fe-Cr based alloys there are two types that seem more suitable as interconnect materials. Ferritic steels and chromium based alloys both have tolerable matching CTEs with SOC components and are therefore the two types of alloys which are most frequently studied [12].

Due to the brittleness well above ambient temperature high chromium content alloys have had limited use as construction material in industrial applications. The company Plansee has however developed oxide dispersion strengthened (ODS) chromium that has substantially improved mechanical properties and their product Ducrolloy is an Cr-5Fe-1Y_2O_3 alloy for SOC interconnects. Chromium based alloys typically have a few percent of iron mixed in to match CTE with SOC components. ODS alloys are quite expensive and difficult to fabricate since powder metallurgical techniques needs to be used [33].

2.6.1 Ferritic stainless steel interconnects

Ferritic refers to the crystal structure of the alloy being body centered just as in ferrous iron. As can be seen in Figure 11 the chromium content must be above 13% for Fe-Cr alloys to be ferritic at all temperatures below the liquidus line. Like chromium based alloys, high temperature grade ferritic steels form a chromia layer that protects against corrosion. To form a single phase chromia layer without any Fe-oxides the chromium content in the alloy needs be at least 17-20% depending on temperature, surface treatment and addition of minor alloying elements and the corrosion resistance generally increases with increasing chromium content [12]. The CTE of ferritic steels decreases with increasing chromium content, however at higher concentration there is a risk of forming an intermetallic σ-phase that causes the alloy to be brittle. The chromium content of commercial ferritic steels for interconnects is typically in the range of 18-26wt%.

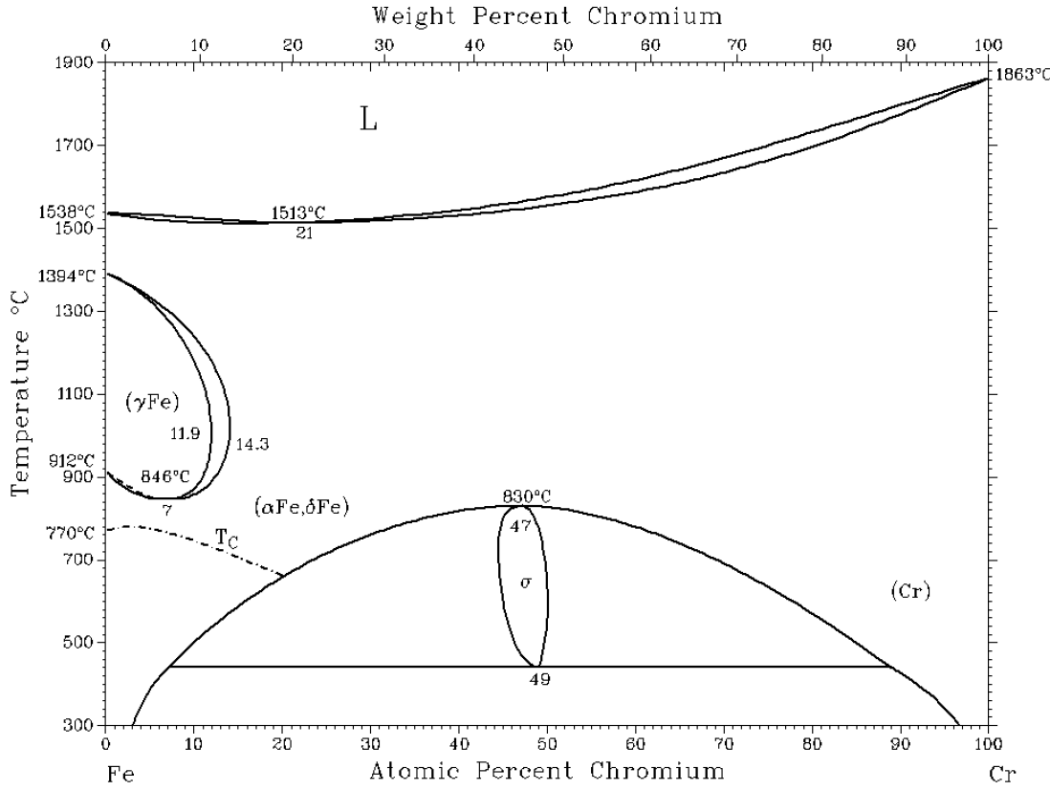

Figure 11. Binary phase diagram of Fe and Cr. α-Fe and δ-Fe are ferritic phases and have BCC structure and γ-Fe is the austenitic phase which has FCC structure.

Ferritic steels have many desirable properties for interconnect applications, are easy to fabricate and have low cost. The main issues with these materials are related to the chromia layer. Chromium oxide scales grow by outward diffusion of chromium ions, which can lead to porosity and buckling of the scale. The result is induced stresses in the scale which may cause cracking and spalling of the scale from the metal. This is devastating from a solid oxide cell point of view since this means that the interconnect will lose contact with the electrodes. The chromia scale must not grow too fast since stack performance depends on the scale being thin enough to still have low electrical resistance. The risk of spallation also increases with increasing scale thickness. Another issue with the Cr_2O_3 scale is that at temperatures above 500°C in oxygen rich environments chromia will start to volatilize and form gaseous chromium species [26] [27]. This will inevitably lead to decreasing chromium content in the material and eventually the chromium concentration will drop below the critical level for formation of a single phase chromia layer and thus the alloy will lose corrosion resistance. Volatile chromium species have been shown to poison the oxygen electrode of SOFCs, thus reducing the efficiency of the stacks significantly [34, 35]. The same effect of chromium poisoning has not been proven for SOEC stacks as of yet, but much fewer studies have been done compared to SOFC. Protective coatings of e.g. cobalt on interconnects can be used to significantly reduce the evaporation of chromium species [36]. Another approach to address the issues mentioned above is by mixing in small amounts of other alloying elements. The section below will briefly go through some alloying elements and their effect on ferritic steel interconnect properties.

2.6.2 Alloying elements in ferritic stainless steel interconnects

2.6.2.1 Si and Al

Silicon and aluminum requires very low oxygen partial pressure to be oxidized and can thus be oxidized internally in the alloy, beneath the protective chromia scale. This internal oxidation has been shown to increase the oxidation rate of chromium oxide scales due to induced internal stresses in the alloy [37]. Si has also been reported to decrease adhesion between the oxide scale and metal and cause the chromia layer to spall of during thermal cycling [12]. The presence of small amounts of Si in interconnect steels can also severely increase the electrical contact resistance due to formation of a continous silica sublayer. This phenomenon can occur even at such low Si concentrations as 0.1wt% [38]. By the same principle alumina layers can also form and decrease conductivity. To avoid internal scales of silica and alumina commercial interconnect steels, like Crofer 22 APU, are alloyed by vacuum melting, which is an expensive process.

2.6.2.2 Refractory elements (Nb, W, Mo)

The elements Nb, W and Mo are classified into a group of hard and heat resistant metals called refractory metals. These elements have been shown to form so called Laves phases which increase the creep strength of ferritic steels, a property that is needed for thin metallic interconnects. The Laves phases are intermetallic precipitates which consist of $(Fe, Cr)_2(Nb, W, Mo)$ and these precipitates increases the hardness of the steel, but also the brittleness [39]. The elements W and Mo do form Laves phases, but their contribution to increased creep strength is mainly attributed to solid solution strengthening due to their large atomic radii [40].

Froitzheim et al. [41] observed increased oxidation rate of a Si free 1%Nb-22%Cr steel, compared to steels that contained higher amounts of Si. The increased growth rate of the chromia scale was concluded to be due to the formation of niobium oxide at the metal/chromia layer interface and Nb was proposed to promote the oxidation of chromium by increasing the diffusion rate of chromium ions due to doping of Cr_2O_3 with Nb. Higher concentrations of Si in the steel were found to suppress this detrimental effect. Silicon dissolves in the $(Fe,Cr)_2Nb$ Laves phases and inhibits the formation of Nb oxide at the scale/metal interface. Thus the combined addition of Si and Nb offers the advantage of higher creep strength for the steel due to Laves phase precipitates formation with reduced tendency for increased oxidation rate. Since Si is dissolved in the Laves phases it is less prone to form an insulating silicon oxide layer and thus due to the presence of Nb additions within the steel, higher Si content can be tolerated. By modification of the alloy chemisty, e.g. by addition of Nb, the tolerance for minor Si levels could be increased and possibly there would be no need for expensive refining steps [42].

2.6.2.3 Ti

Like aluminum and silicon, the presence of titanium in the alloy results in internal oxidation. The internal titanium oxide zone can have the beneficial effect of strengthening the near-oxide scale area and can prevent scale buckling [25]. Ti also reduces contact resistance of the scale due to a doping effect of chromium oxide [43]. However, the diffusion of Cr ions is also increased by this doping effect, which results in higher growth rate of the chromia scale. Too high concentrations of Ti may also lead to spallation of the chromia scale. Pirón and Quadakkers reported that 0.15wt% Ti caused severe internal oxidation at the grain boundaries resulting in plastic deformation and buckling of the oxide scale [44].

2.6.2.4 Mn

Manganese has become a standard alloying element in commercial ferritic steels for SOC interconnects. Mn diffuses through the oxide layer and results in a two phase protective oxide layer with $MnCr_2O_4$ spinel on top and Cr_2O_3 below[25].This chromium manganese spinel substantially lowers the rate of evaporation of chromium species from the steel substrate [45], which are known to poison the oxygen electrode of SOFCs and deplete the alloy from chromium. Additionally, the introduction of a $MnCr_2O_4$ spinel layer increases the conductivity of the oxide scale for the interconnect [46].

2.6.2.5 Reactive elements(RE)

Oxygen active elements such as yttrium, hafnium, cerium, lanthanum and zirconium are known to have very beneficial effects on the oxidation behavior of chromia forming alloys [47]. In high temperature corrosion science these elements are often referred to as reactive elements and their influence on the oxidation behavior is called the reactive element effect. Small additions of these elements to a chromia forming alloy greatly increases the adherence of the chromia scale to the metal [21]. Additionally, reactive elements significantly decrease the chromium oxide growth rate and enhance the selective oxidation of chromium, thus restricting the formation of iron oxides. The latter effect makes it possible to use less chromium in alloys and yet form a protective chromia scale. Or if the same amount of chromium is used in an alloy the oxide scale will form faster in the presence of added REs.

The oxidation mechanism of chromium is also altered when reactive elements are present, from predominant outward cation diffusion to oxygen inward transport [48]. Even though the RE effect has been known for more than 70 years the mechanism behind it is still in debate. The effect has been studied extensively and suggested mechanisms include segregation of RE to the oxide grain boundaries which reduces cation transport, tying up sulfur which prevents it to accumulate at the scale/metal interface and weaken adhesion. It has also been shown that REs are effective both when added as metal or oxide dispersion to an alloy and even when applied to a metal or oxide surface [21]. As a consequence of reactive element doping the contact resistance of a metal interconnect can be improved. Studies with Y doping has shown that contact resistance of decreases compared to undoped alloys due to the decreased growth rate and improved adhesion of the chromia scale [29].

2.7 Degradation of SOEC

Temperatures between 600-1000°C are necessary to achieve sufficient reaction kinetics and conductivity within cell stacks, but these high temperatures also speed up chemical side reactions and other degrading processes. Durability of electrolyzers has been pointed out as one of the main factors that affect hydrogen cost [11]. Hence there are strong incentives towards developing more long lasting SOEC stacks. Degradation phenomena of SOC stacks have been more studied for units run in SOFC mode than in SOEC mode. Even if the operation is different, the knowledge from SOFC testing can in many cases be transferred to SOEC technology. Currently SOC stacks degrade more in SOEC mode than in SOFC mode [49]. Some known degradation phenomena for SOEC includes delamination of oxygen electrodes, coarsening of nickel particles in the fuel electrode, loss of ionic conductivity in the electrolyte, formation of inhibiting species due to migration of ions from interconnects and increase of ohmic resistance due to oxide scale build up on metallic interconnects [8, 49]. Chromium evaporation is known to be a major problem in SOFC stacks since volatile chromium is gets

deposited on the cathode and poisons the oxygen electrode. This phenomenon is less studied for SOEC mode but is suspected to be less detrimental to stack performance.

3 Experimental

3.1 Material

The following materials were studied: AL441 HP (ATI), Sanergy HT (Sandvik), Crofer 22H (ThyssenKrupp) and E-brite (ATI). Composition and thickness of the steels are displayed in Table 1. Sanergy HT was tested both uncoated and coated with 10 nm Ce and the coating was applied by Sandvik Materials Technology AB.

Table 1. Composition of the investigated steels in weight%. The compositions were given by the respective manufactures for the received batches.

Material	Fe	Cr	C	Mn	Si	Al	W/Mo	Nb	RE
Sanergy HT[a]	Bal	21.2	0.040	0.3	0.12	0.02	0.96 Mo	0.71	Zr
Crofer 22H[a]	Bal	22.9	0.007	0.4	0.2	0.02	1.9 W	0.5	La
E-brite[b]	Bal	26.2	0.002	0.073	0.17	0.02	1.02Mo	0.12	
AL 441 HP[b]	Bal	17.8	0.013	0.29	0.38	0.03		0.50	

a) Sample thickness of 0.2mm
b) Sample thickness of 0.5mm

3.2 Exposures

In this study oxidation behavior of four different commercial SOFC grade ferritic steels have been investigated, to test their suitability for use in as interconnects in SOEC stacks. Gravimetric studies as well as chromium evaporation measurements have been performed. All steels were obtained in sheets from the respective manufactures and sample coupons of 15x15 mm were cut out with scissors. The samples were washed first in acetone in an ultrasonic bath for 10 minutes and subsequently in high purity ethanol for an additional 10 minutes. The samples have been exposed at 850°C in tube furnaces under different atmospheres. The coupon samples were placed parallel to the flow in an alumina holder with slits (Figure 12). The total gas flow rate was 1000 ml/min in all experiments, which corresponds to a mean flow velocity of 3.8 cm/s inside the reaction chamber.

In the gravimetric tests six samples were exposed simultaneously: one sample of each of the five different interconnect materials from Table plus an additional sample of Sanergy HT for internal deviation reference. It was the intention that by testing all the steels at once in each specific exposure, comparison of the results between the materials would be become more credible, since test-to-test variations in exposure environment can be ruled out. These tests were carried out discontinuously, meaning that the furnace was cooled down to room temperature before each gravimetric measurement. After weighing the samples they were placed back in the furnace and the experiment was continued.

3.2.1 Oxygen side exposures (gravimetric)

Exposures of all the steels in Table have been performed in three different oxygen pressures: 100% oxygen, 1% oxygen diluted with argon and 0.01% oxygen diluted with argon. Exposures have been replicated three times in 100% oxygen, two times in 1% oxygen and one time in

0.01% oxygen and different furnaces were used. The experiments were carried out in tubular silica glass chambers with 46 mm inner diameter. Pictures of the experimental setup are displayed in Figure 12. Oxygen environments of different concentrations were chosen to be able to investigate the corrosion behavior as functions of oxygen partial pressures. The motivation for studying oxygen concentration dependence comes from recent studies with SOEC high pressure systems, e.g. ref. [5]. The diluted oxygen environments were chosen as they are experimentally easier and more safe to perform than exposures at high pressures.

The diluted oxygen environment was obtained by mixing oxygen and argon at the inlet of the reaction chamber by controlling the flow rate of the two gases with adjustable valves. Pure oxygen with flow rate of 10ml/min was mixed with pure argon with flow rate of 990ml/min for the 1% oxygen exposures. To obtain 0.01% oxygen environments premixed 1%O_2-Ar was used instead of pure oxygen in order to be able to regulate the oxygen flow more precisely.

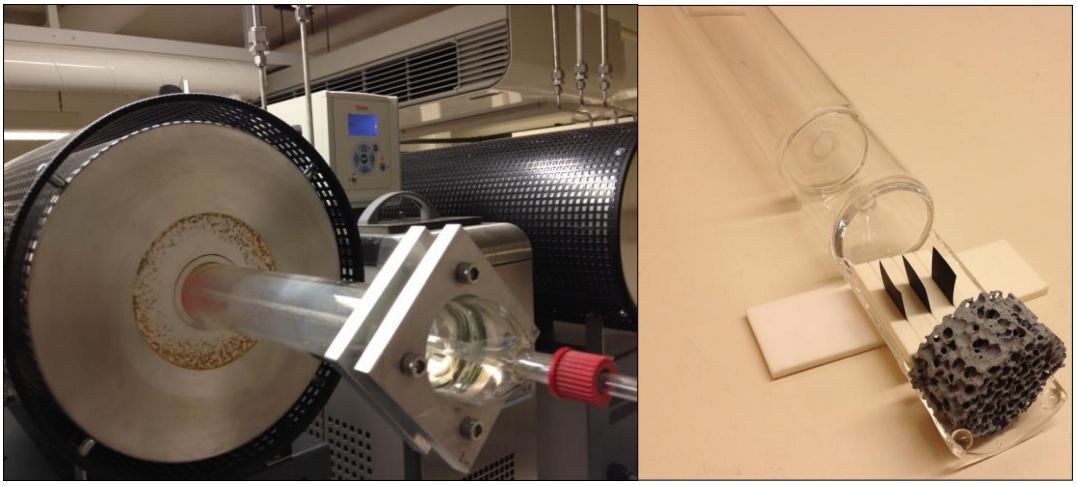

Figure 12. Pictures and schematics of the experimental setup. Left: tube furnace with silica reaction chamber and inner tube used for the exposures in oxygen. Right: silica inner tube mounted with three samples and a SiC foam behind the samples for a more even flow profile.

3.2.2 Fuel side exposures (gravimetric)

To replicate fuel side, or cathode, conditions in an SOEC stack, exposures with an atmosphere containing a mixture of 3% hydrogen and 34% water vapour diluted with argon were performed three times. An alumina tube was used as reaction chamber instead of a silica tube to avoid silica volatilization in low pO_2 atmosphere. The experimental setup is displayed in Figure 13. The sample holder was inserted directly into the alumina tube and no inner tube was used. To achieve an atmosphere of 34% H_2O, premixed 5% H_2-Ar gas was bubbled through a humidifier and led through a condenser set at a temperature of 72.0°C. The gas tube connecting the condenser and the reaction chamber was heated above 100°C with a heating cord to ensure that no condensation occurred. During exposure the condenser was refilled with deionized and deaerated water through a siphon tube that allowed the condenser to be refilled with minimal exposure to air. The water was deaerated by bubbling nitrogen gas through a siphon bottle.The system was flushed with 5% H_2-Ar gas at room temperature before the furnace was started to reduce the oxygen partial pressure to negligible levels prior to exposure.

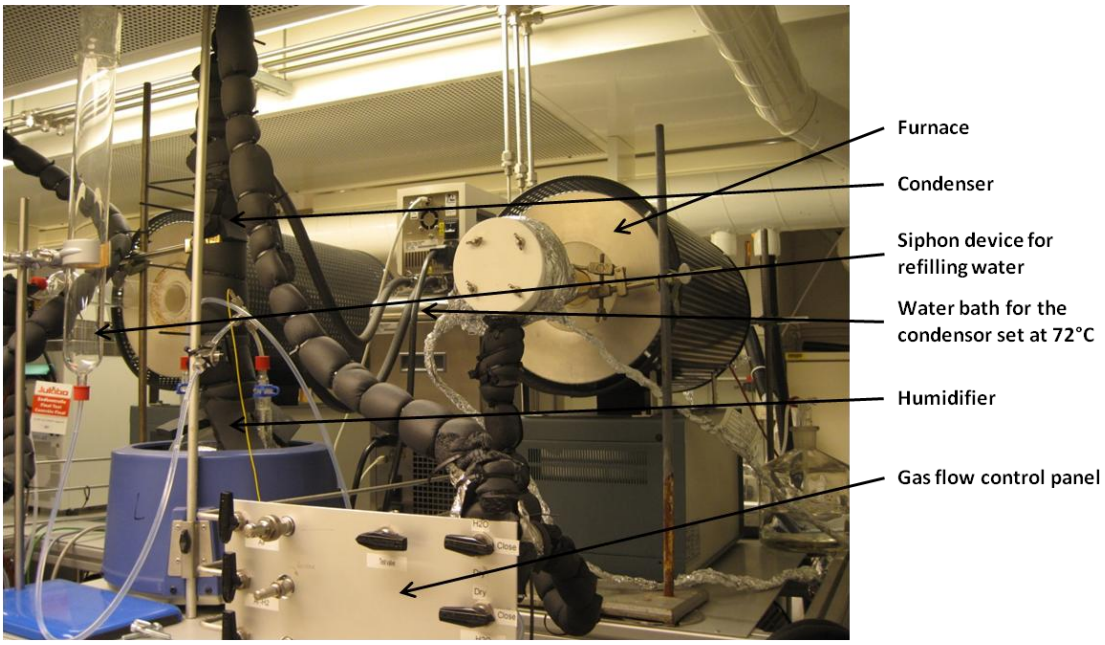

Figure 13. Experimental setup for the experiments run in 3% H_2 - 34% H_2O atmosphere.

3.2.3 Chromium evaporation

Chromium evaporation has been measured in 100%, 50% and 25% oxygen atmospheres to study the dependence on oxygen partial pressure. Three samples of Crofer 22H were used in each test and the exposures were run continuously for 168h. After exposure after the amount of collected volatile chromium species was measured. The samples were also weighed before and after exposure. Two exposures in 25% oxygen were performed and three in 50%. Due to lack of equipment and project time one exposure was performed in 100% oxygen.

The setup for the chromium evaporation experiments was the same as the system presented in Figure 12 but also included a 6 mm inner diameter alumina denuder tube downstream of the samples (see Figure 14). The denuder tube was coated with Na_2CO_3 in order to collect volatile chromium species according to the following reactions:

$$CrO_2(OH)_2(g) + Na_2CO_3(s) = Na_2CrO_4(s) + H_2O(g) + CO_2(g) \quad (18)$$

$$CrO_3(g) + Na_2CO_3(s) = Na_2CrO_4(s) + CO_2(g) \quad (19)$$

The tube was subsequently rinsed with MQ water to leach out the deposited sodium chromate which was quantified by spectrophotometry. A more detailed description of the denuder technique can be found elsewhere [50].

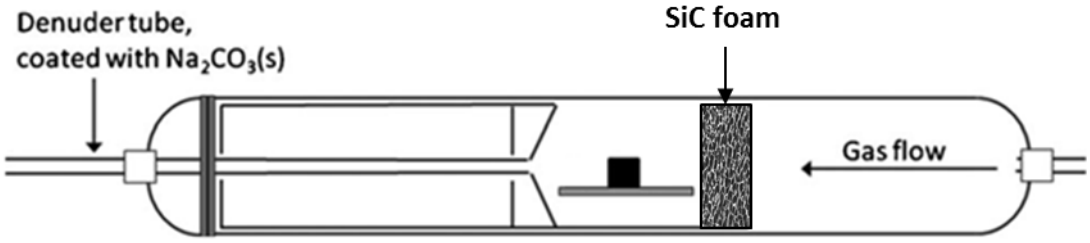

Figure 14. Schematic illustration of the setup for chromium evaporation measurement. A denuder tube coated with Na_2CO_3 is inserted into the reaction chamber and inner tube to collect volatile chromium species. A foam structure of SiC evens out the flow profile and reduces natural convection.

3.3 Analysis

Analysis of the samples included gravimetric measurements, SEM investigation, EDX and XRD analysis and spectrophotometry. To study oxide growth rate samples were weighed on a six decimal Sartorius balance. At each occasion the samples were weighed twice and the average value was used. Plan view images of the samples' surface microstructure and atomic contrast obtained by Scanning Electron Microscopy in a FEI Quanta FEG 200 ESEM and a Leo Ultra 55 SEM. Connected to this microscope is an Oxford Inca EDX system which was used for elemental analysis. Chromium content from denuder tubes was measured by spectrophotometry using a Thermo Scientific Evolution 60s UV-visible spectrophotometer.

3.3.1 Calibration of spectrophotometer

The maximum light absorbance for chromate in solution is at 370 nm wavelength, which was the setting used for all analyses. A standard curve for chromate solution was made in order to quantify the chromium in the sample solutions. From a 1/60 M $K_2Cr_2O_7$ standard solution, 11 different chromate solutions were prepared. The solutions were prepared by diluting the mother solution with 0.5 M NaOH to ensure high pH of the solutions. This is important since the equilibrium between chromate and dichromate (20) needs to be shifted so that chromate ions are predominant since the dichromate ion does not have the same maximum absorbance wavelength.

$$2CrO_4^{2-} + 2H^+ \leftrightarrow Cr_2O_7^{2-} + H_2O \quad (20)$$

Fournier-Salaün et al. have done studies regarding chromate quantification by spectrophotometry and found that pH 9 and above is sufficient for almost 100% chromate predominance [51]. By testing with indicator paper it was confirmed that the sample solutions from the leached denuders were sufficiently alkaline for the equilibrium to be shifted against chromate ion predominance. Due to the high alkalinity of sodium carbonate the sample's pH should not be an issue. Each specific chromate solution was measured twice and the resulting standard curve is presented in Figure 15. The absorbance shows linear dependence on concentration which is on good agreement with the Lambert Beer's relation

$$A = \varepsilon * l * c \quad (21)$$

where A is the absorbance, ε the molar absorbtivity, l the pathlength of the light through the solution and c concentration. In this case l is a constant since only one type of cuvette fits into the spectrometer, thus the absorbance dependence on concentration can be derived from the standard curve and expressed as

$$A = 0.0902 * c \quad (22)$$

if concentration is expressed in weight ppm of chromium.

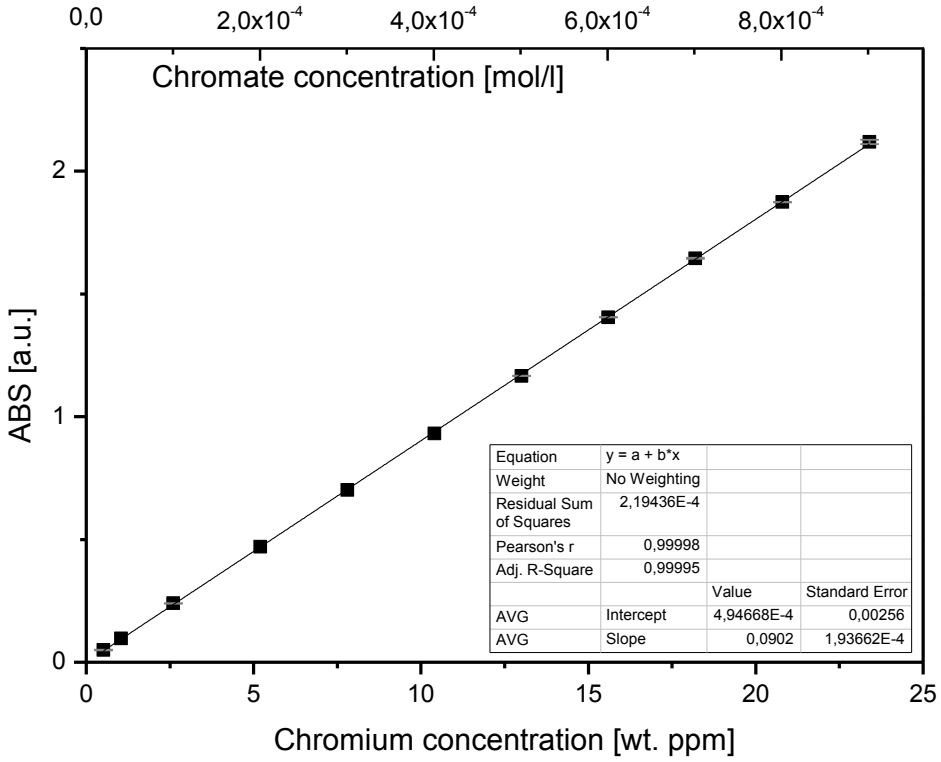

Figure 15. Chromate and chromium concentration plotted against absorbance.

4 Results

4.1 Gravimetrical investigations

Mass gains of all samples have been measured discontinuously and are plotted as functions of time in Figure 16-19. The mass gain is due to uptake of O_2 during oxidation and is thus a measure of corrosion rate. In dry 100% oxygen exposures (Figure 16) Crofer 22H has the highest observed oxidation rate with an average mass gain of 0.83mg*cm^{-2} after 500h, closely followed by AL 441 HP at 0.79mg*cm^{-2}. Uncoated Sanergy HT performs better than these two steels in terms of oxidation rate and it is also seen that the cerium coating effectively reduces oxidation, since the mass gain after 500 h is reduced from 53 to 40mg*cm^{-2}. The gravimetric result from E-brite in 100% oxygen is the lowest observed with 37mg*cm^{-2} after 500h, but a SEM investigation revealed that tiny flakes of the oxide scale had spalled of from these samples (see Figure 20). This means that not all the oxide is weighed and the observed mass gain is not in direct proportion to oxidation of the steel. No spallation was observed for any of the other samples in this environment.

The mass gains in 1% oxygen (see Figure 17) after 500 h are ranging from 0.40 to 1.05mg*cm^{-2} for Ce coated Sanergy HT and Crofer H respectively. The oxidate rate of uncoated Sanergy HT is higher than for Ce coated, but significantly lower than for AL 441 HP which has similar oxidation rate as Crofer 22H. A mass loss was observed for E-brite between 48h and 500h which was due to severe spallation of the oxide scale during cool down of the furnace to room temperature (see Figure 20). Exposures have also been carried out in 0.01% oxygen (Figure 18). The results from this exposure are similar to those in 1% and 100% oxygen with the highest mass gain observed after 500h being 0.91 mg*cm^{-2} for Crofer 22H and the lowest 0.35mg*cm^{-2} for Ce coated Sanergy HT. Higher oxidation rate is observed for uncoated than Ce coated Sanergy HT and AL 441 HP has similar oxidation rate as Crofer 22H. In 1% oxygen E-brite was spalling severely which resulted in mass loss after each measurement point after 48h.

To simulate the environment of the fuel side of an SOEC stack, exposures have been carried out in 34% steam and 3% hydrogen in argon (see Figure 19). In this environment the highest oxidation rate was observed for AL 441 HP with an average mass gain of 1.90mg*cm^{-2} after 500 h, which was significantly higher than for the other tested steels. Due to the large increase in oxide thickness of AL 441 HP during fuel side exposures some errors when weighing the samples occurred, since some oxide traces were left stuck in the slits of the alumina sample holders. Minor spallation at the edges of the AL 441 HP samples was also detected after exposure in fuel side environment. The lowest oxidation rate in this environment was observed for Ce coated Sanergy HT which had a mass gain of 0.36mg*cm^{-2} after 500h. The oxidation rate of Sanergy HT with cerium coating was closely matched with that of E-brite. Mass gains of Crofer 22H and Sanergy HT were very similar after 500h and slightly higher than that of E-brite.

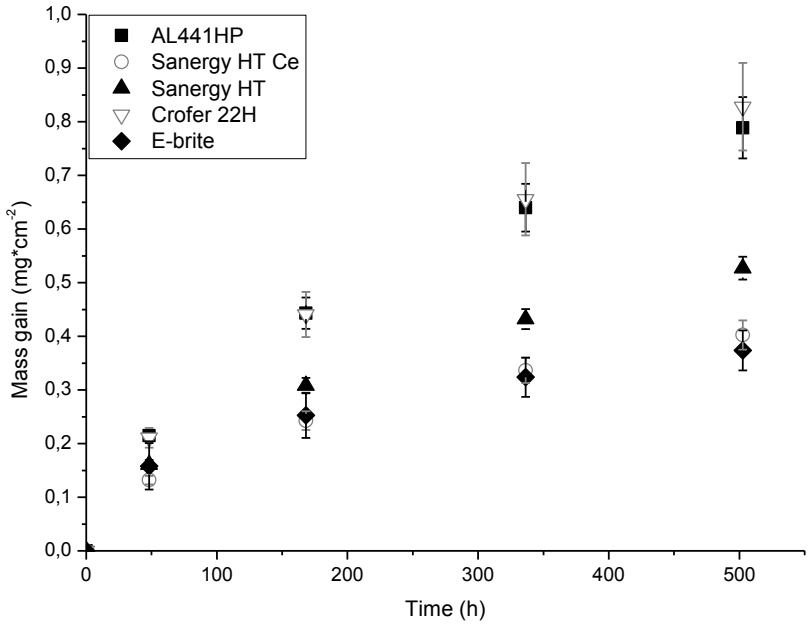

Figure 16. Mass gain as a function of exposure time for AL 441 HP, Sanergy HT Cerium coated, Sanergy HT, Crofer 22H and E-brite in 100% oxygen at 850°C.

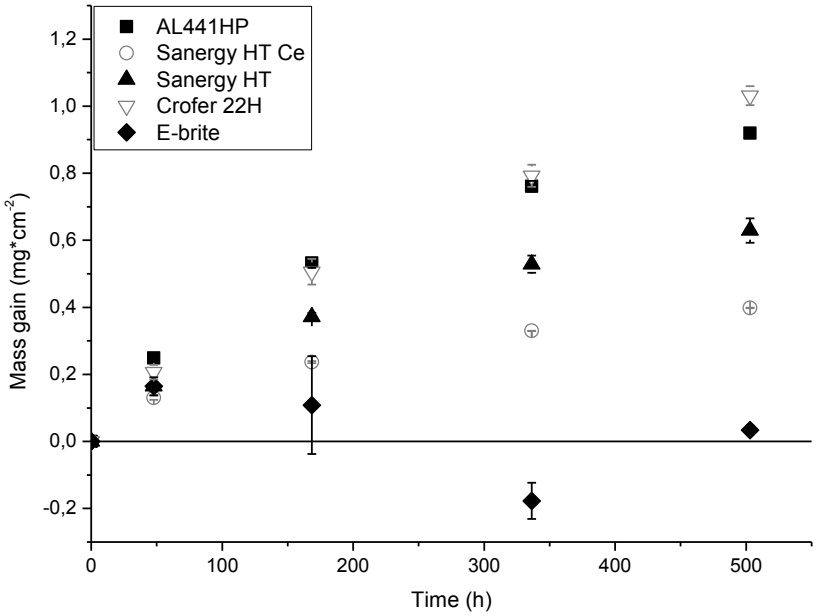

Figure 17. Mass gain as a function of exposure time for AL 441 HP, Sanergy HT Cerium coated, Sanergy HT, Crofer 22H and E-brite in 1% oxygen diluted with argon at 850°C.

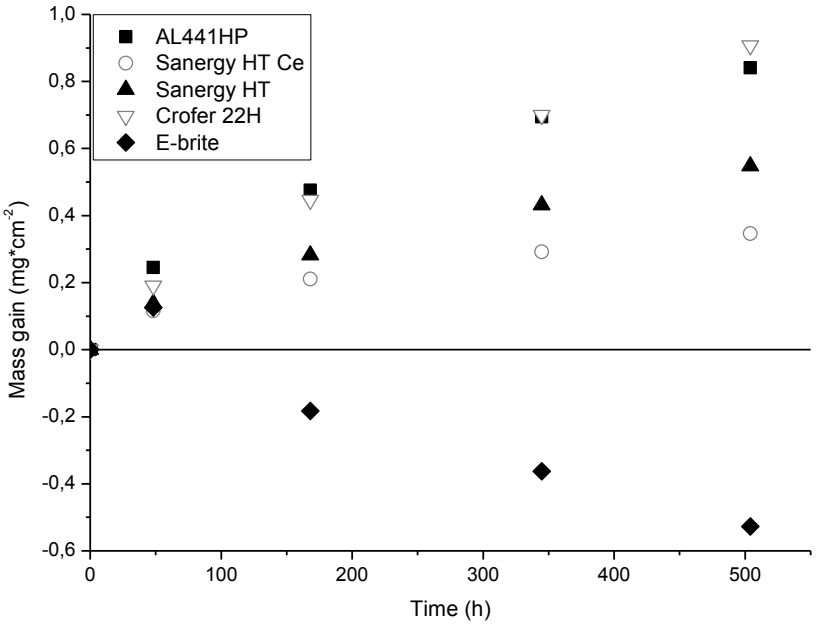

Figure 18. Mass gain as a function of exposure time for AL 441 HP, Sanergy HT Cerium coated, Sanergy HT, Crofer 22H and E-brite in 0.01% oxygen diluted with argon at 850°C. This experiment has only been performed once, hence the lack of error bars in the graph.

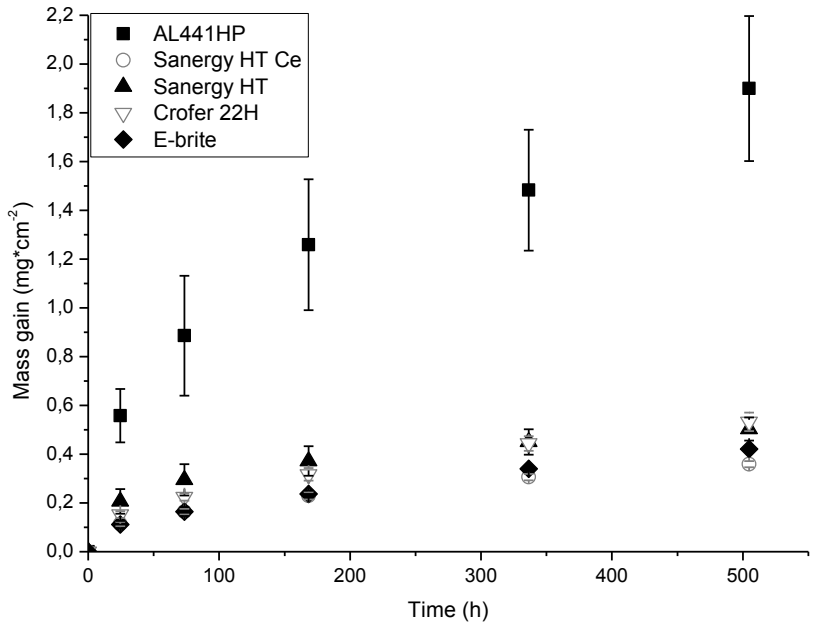

Figure 19. Mass gain as a function of exposure time for AL 441 HP, Sanergy HT Cerium coated, Sanergy HT, Crofer 22H and E-brite in 34% steam and 3% hydrogen diluted with argon at 850°C.

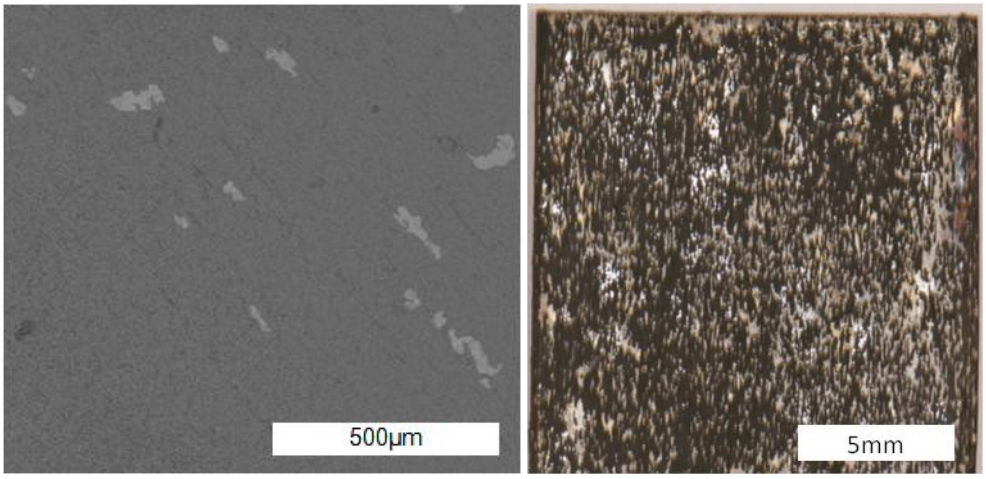

Figure 20. Left: SEM image of an E-brite sample exposed in 100% oxygen for 500h. Right: Photograph of an E-brite sample exposed for 168h in 1% oxygen. Oxide flakes have spalled off during cooling down from 850°C to room temperature.

Figure 21 summarizes the results of the oxidation rates in all the exposures. In direct comparison of the dry oxygen containing environments a small increase in oxidation rate for the samples exposed in 1% oxygen compared to 100% oxygen can be observed for all materials. In oxygen partial pressure of 0.01% the oxidation rates seem to be lower than in 1% oxygen, thus breaking any trend towards increased oxidation rate with reduced oxygen partial pressure. It should be noted here, that the exposure with 0.01% oxygen was only performed once. Almost the same internal order between the tested materials in terms of oxidation rate is observed in 100%, 1% and 0.01% oxygen environments. An exception was E-brite which spalled more severely during thermal cycling in the argon diluted oxygen atmospheres. This resulted in mass losses between some measurements in 1% oxygen and even larger mass losses in 0.01% oxygen.

A second set of isothermal exposures of Crofer 22H were carried out for 168 h at 850 °C in argon with oxygen contents of 25%, 50% and 100%. The main purpose of this experiment was to measure chromium evaporation (see section 4.3), however the mass gain after 168h for the Crofer 22H samples are plotted in Figure 22. From this data no trend in mass gain against oxygen partial pressure can be concluded.

By overall comparison of oxidation rates in oxygen and fuel side exposures it can be seen that Ce coating effectively decreases oxidation rates of Sanergy HT in all environments. E-brite samples showed substantially improved corrosion performance in fuel side exposures compared to oxygen exposures, with low oxidation rate and no indications of spallation. The oxidation rate of Crofer 22H was also significantly lower in fuel side exposures and similar to that of Sanergy HT, which had almost the same mass gain after 500h in oxygen and fuel side exposures. The only exception to having improved or unchanged corrosion performance in this atmosphere was AL 441 HP which had significantly higher oxidation rate in steam with hydrogen atmosphere.

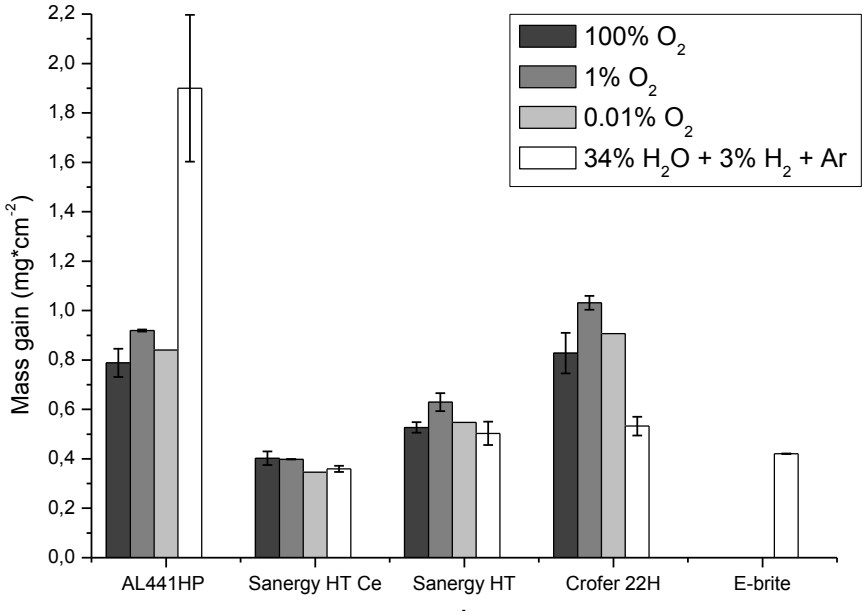

Figure 21. Mass gain after 500h exposure. The results for the material E-brite exposed in oxygen has been omitted due to spallation which gave misleading mass gain results.

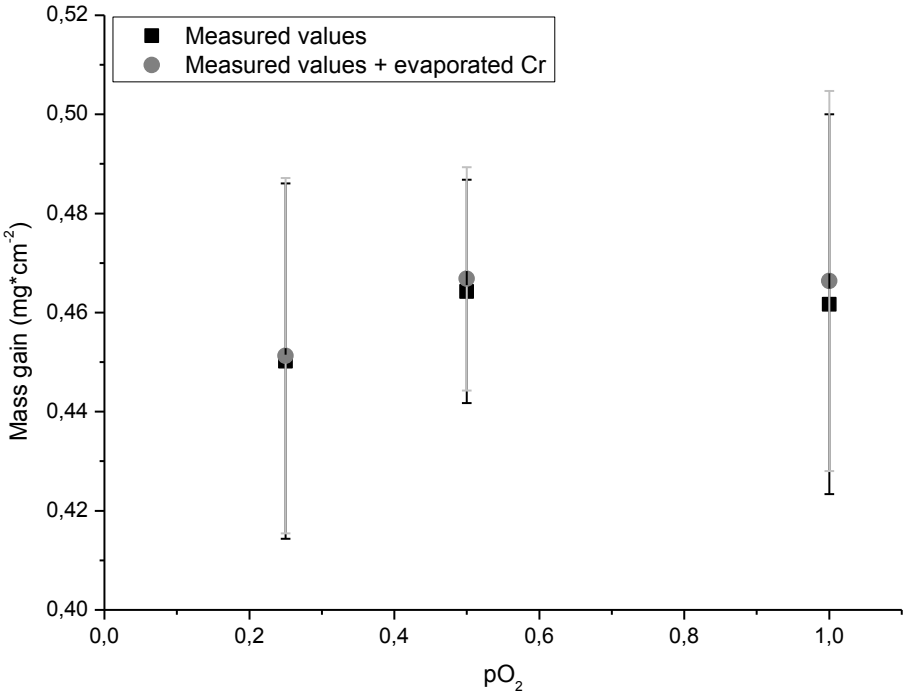

Figure 22. Mass gain of samples used in the chromium evaporation experiment. The samples have been exposed isothermally for 168h at 850°C. The mass gain for 100% partial pressure includes data from the gravimetrical experiments. In the gray points the mass of collected volatile chromium species have been added.

The oxide kinetics of most of the exposed steels can be described by parabolic growth rate and thus Wagner's oxidation model, with oxide thickness exchanged for mass gain, can be used:

$$\left(\frac{\Delta m}{A}\right)^2 = k_p t \quad (23)$$

where Δm is change in mass, A is total sample area, t is the exposure time and k_p the parabolic oxide rate constant [22]. Squared mass gains as a function of exposure time are presented in Figure 23-26. E-brite has been omitted from the parabolic plots from the oxygen exposures as it suffered severe spallation in 1% and 0.01% oxygen and did not follow parabolic growth rate in 100% oxygen environment. Furthermore, AL 441 HP has been omitted from the H_2O/H_2 plot due to spallation and too large deviations. As can be seen in Figure 26, uncoated Sanergy HT does not follow parabolic oxidation rate in fuel side conditions, thus no k_p value could thus be retrieved. Furthermore, the oxidation rate Crofer 22H can be argued to differ slightly from the parabolic rate law in oxygen side exposures.

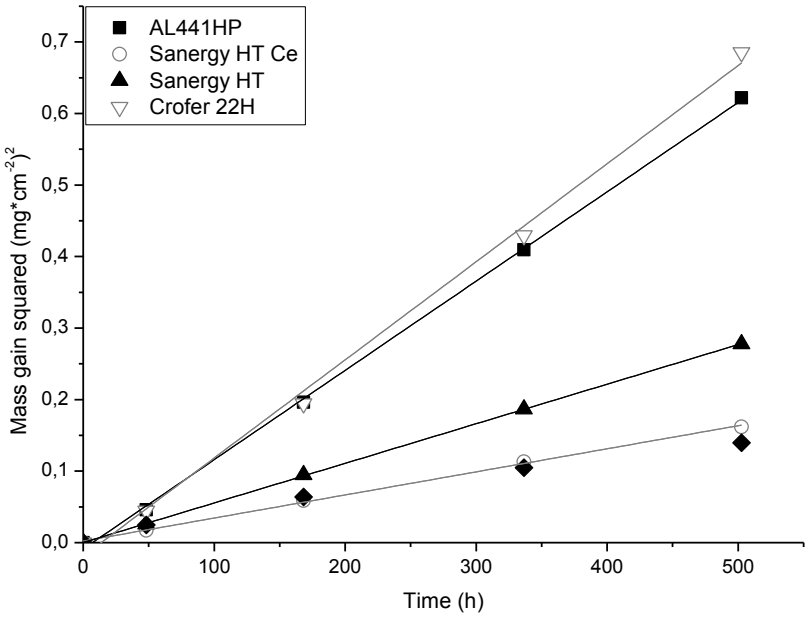

Figure 23. Mass gain squared as a function of exposure time for AL 441 HP, Sanergy HT Cerium coated, Sanergy HT, Crofer 22H in 100% oxygen at 850°C.

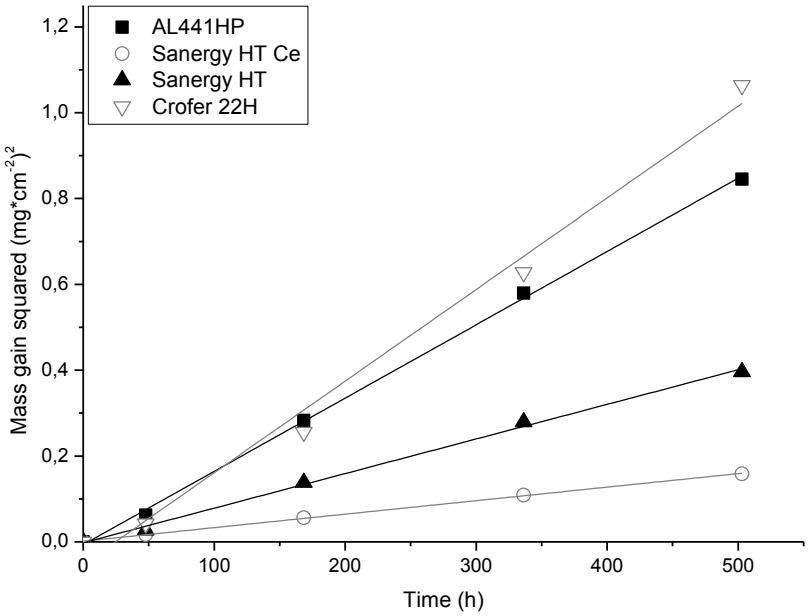

Figure 24. Mass gain squared as a function of exposure time for AL 441 HP, Sanergy HT Cerium coated, Sanergy HT, Crofer 22H in 1% oxygen at 850°C.

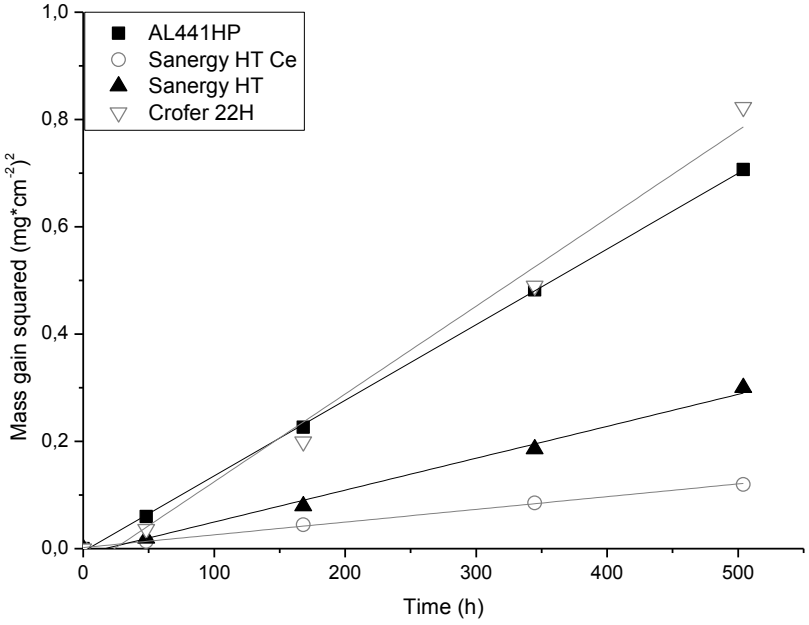

Figure 25. Mass gain squared as a function of exposure time for AL 441 HP, Sanergy HT Cerium coated, Sanergy HT, Crofer 22H in 0.01% oxygen at 850°C.

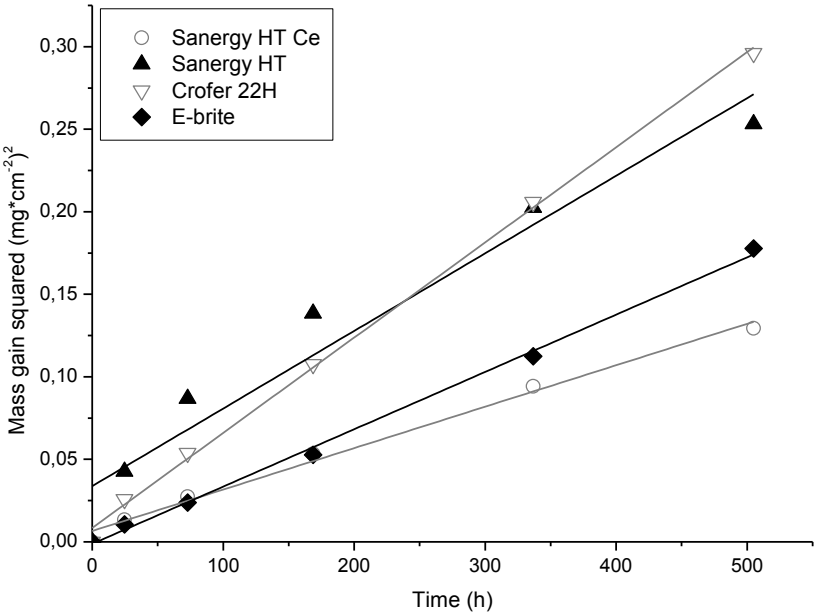

Figure 26. Mass gain squared as a function of exposure time for AL 441 HP, Sanergy HT Cerium coated, Sanergy HT, Crofer 22H in steam/hydrogen at 850°C.

The corresponding parabolic rate constants from the parabolic plots in Figure 23-Figure 26 are presented in Table 2. Some materials did not follow the parabolic rate law due to reasons mentioned above and their k_p values could thus not be retrieved. For the alloys that exhibited parabolic oxidation rates it is possible to predict the mass gains at the time t in the respective atmospheres according to (23).

Table 2. Parabolic oxide growth rate constants (k_p) for the studied interconnects. Some values have been omitted due to non-parabolic growth rate.

	k_p*10^{14} [$g^2cm^{-4}s^{-1}$]				
	AL441HP	**Sanergy HT Ce**	**Sanergy HT**	**Crofer 22H**	**E-brite**
100% O_2	35	9	15	38	-
1% O_2	47	9	22	59	-
0.01% O_2	40	6	17	48	-
H_2O/H_2	-	7	-	15	10

4.2 Morphology and microstructure

SEM plan view images of the samples exposed in 100% oxygen, 1% oxygen and in 34% water and 3% hydrogen were taken after 500 h exposure. Images of all materials exposed 100% oxygen are presented in the left column of Figure 27. All materials exhibited relatively large crystals in this atmosphere, with maximum crystal sizes ranging from 1-4µm for Sanergy HT and E-brite respectively. The smallest crystallites after exposure in 100% oxygen were found on Sanergy HT with Ce coating. These small crystallites appear bright in the BSE image since they are rich in Ce (which has a high atomic number compared to the rest of the oxide). Occasional larger octahedral shaped crystals of up to 4µm were also found on the Ce coated Sanergy HT

samples exposed in 100% oxygen. The morphologies of AL 441 HP, Crofer 22H and Sanergy HT are similar in this environment, with tetrahedral and octahedral shaped crystals with sizes of approximately 0.5-2 µm. On the E-brite samples larger oxide flakes of up to 4µm were observed after exposure in 100% oxygen.

In the right column of Figure 27 SEM images of the surface morphology of all the samples exposed in 1% oxygen are presented. After exposure in this environment, the crystals on the surface of the samples were smaller than those formed in 100% oxygen for all materials but the shape of the crystals looked similar. The sizes of the largest crystals formed in 1% oxygen varied from approximately 0.4-1µm for Sanergy HT and AL 441 HP respectively. The cerium coated Sanergy HT samples exhibited Ce rich crystals on the surface that appeared bright in the BSE image. To verify that these crystals were really on the surface, low voltage SEM analyses with a backscattered in-lens detector were performed which concluded that the cerium rich crystals were present at the very surface of the samples (see Figure 28).

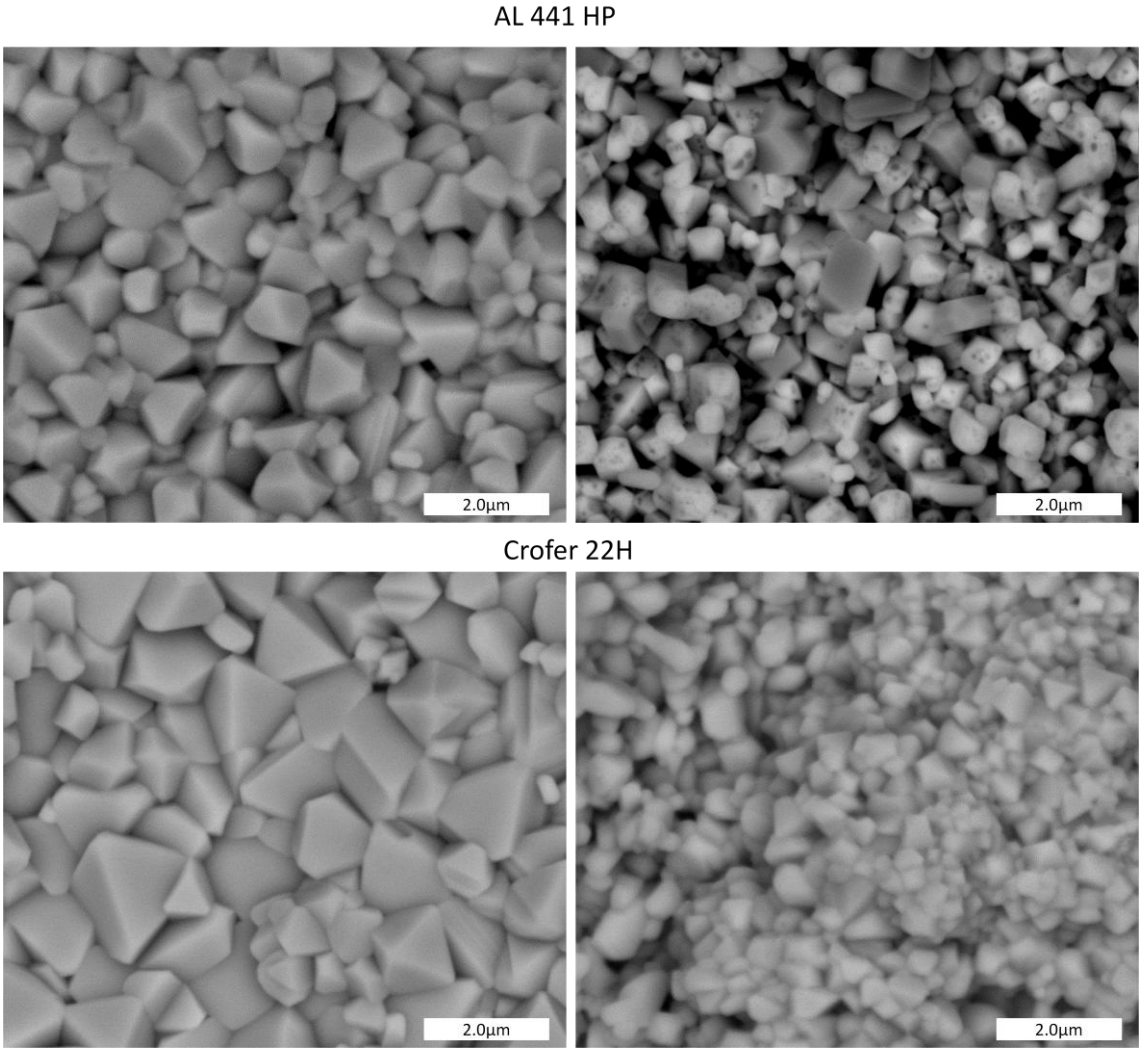

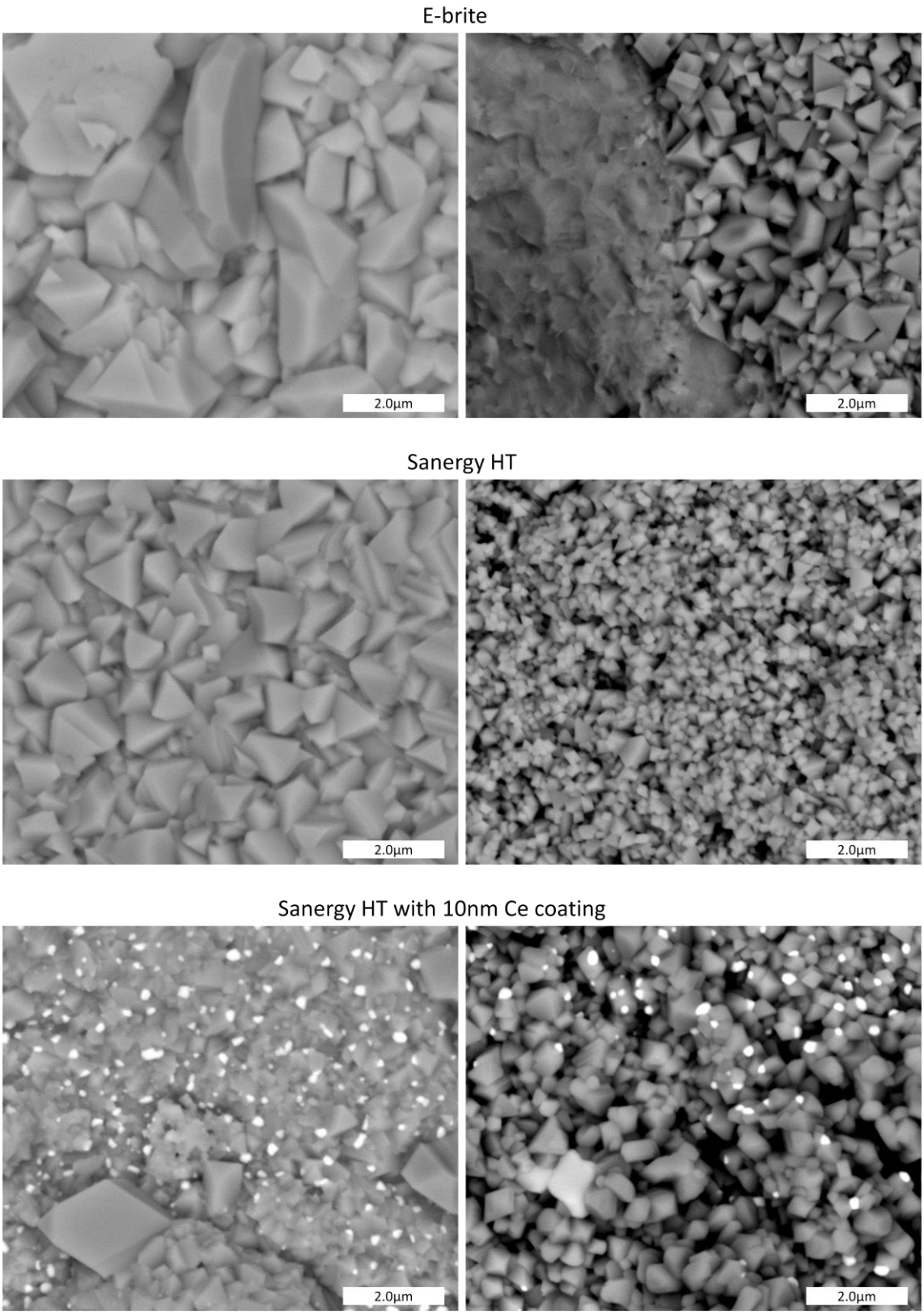

Figure 27 SEM backscattered images of AL 441 HP, Crofer 22H, E-brite, Sanergy HT and cerium coated Sanergy HT after 500h exposure in 1% oxygen (left) and 100% oxygen (right) at 850°C.

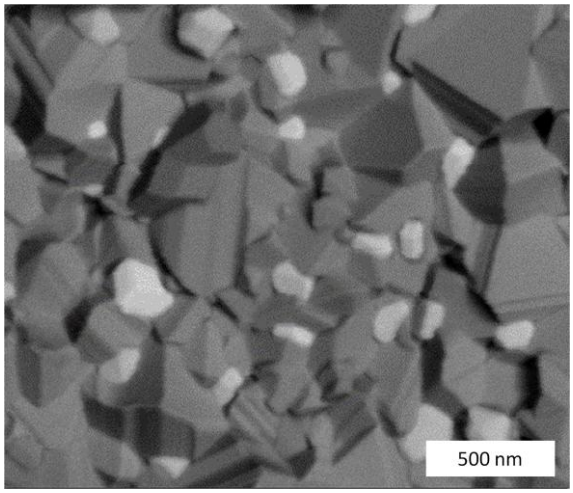

Figure 28. SEM backscattered images of Sanergy HT with 10 nm cerium coating after 500 h exposure in 100% oxygen at 850°C. The image was taken with in-lens back scattered detector at 1kV acceleration voltage and a voltage bias set at almost the same potential, which means that only the top surface will be analyzed.

In Figure 29 and Figure 30 plan view images of all the samples exposed in 34% steam and 3% hydrogen are presented. The surface morphology of the samples exposed in fuel side atmosphere differed from those exposed in oxygen. The morphology also differed amongst the different materials in this environment. Crofer 22H and E-brite formed lamella shaped crystallites that were approximately 1µm long and a few tens of nm thick, whereas the surface morphology of Sanergy HT consisted of less defined and less sharp crystallite with sizes up to 500nm. Furthermore, the oxide layer on AL 441 HP lacks defined grain structure and has quite open structure morphology after exposure in fuel side atmosphere. Cerium rich oxides were found on cerium coated Sanergy HT samples that had been exposed in fuel side conditions, although in less quantity than on samples exposed in oxygen side conditions. Contrary to the uncoated Sanergy HT samples, the cerium coated samples had formed whisker type crystallites of slightly smaller sizes than those found on E-brite and Crofer 22H.

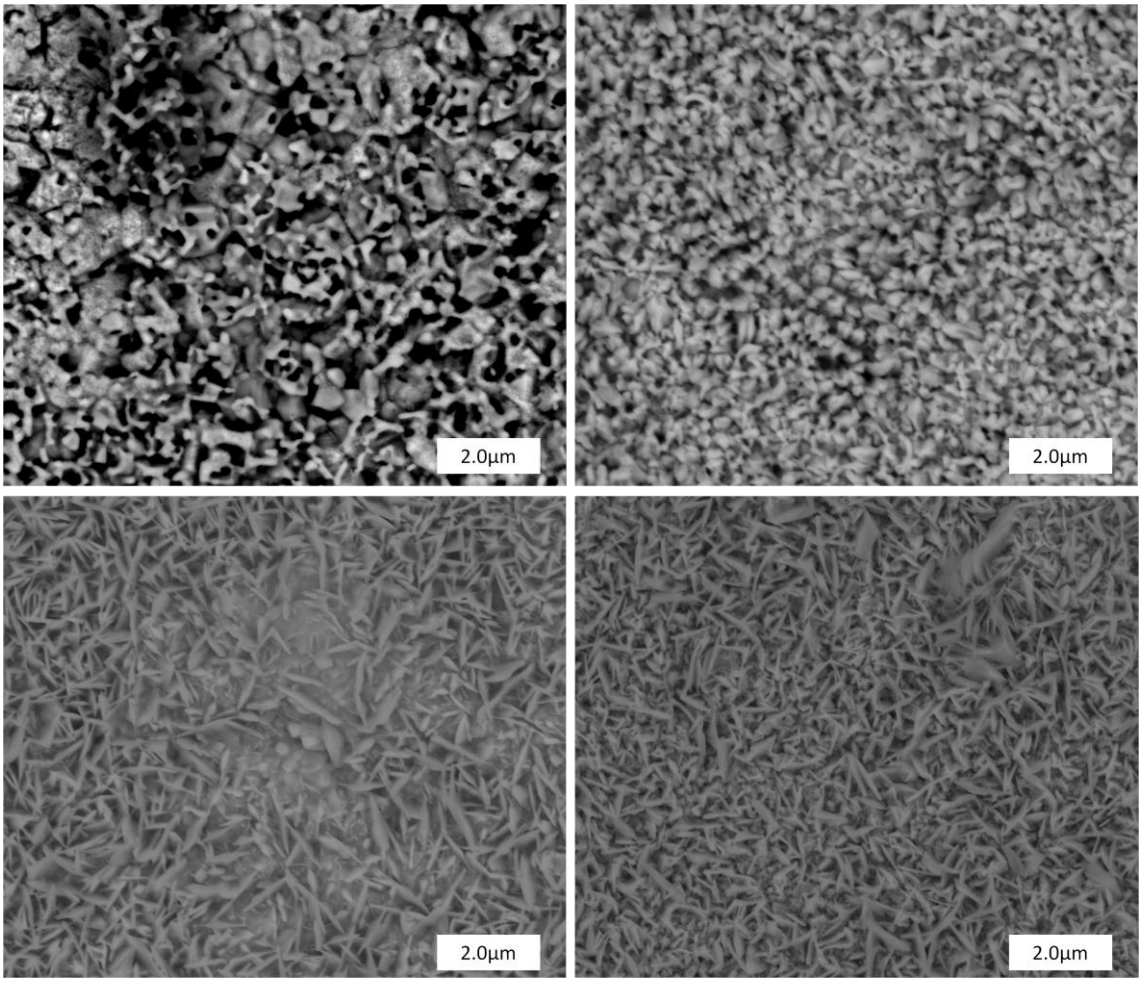

Figure 29. SEM backscattered images of samples exposed in 34% steam and 3% hydrogen at 850°C. Top left: AL 441 HP, top right: Sanergy HT, bottom left: Crofer 22H, bottom right: E-brite.

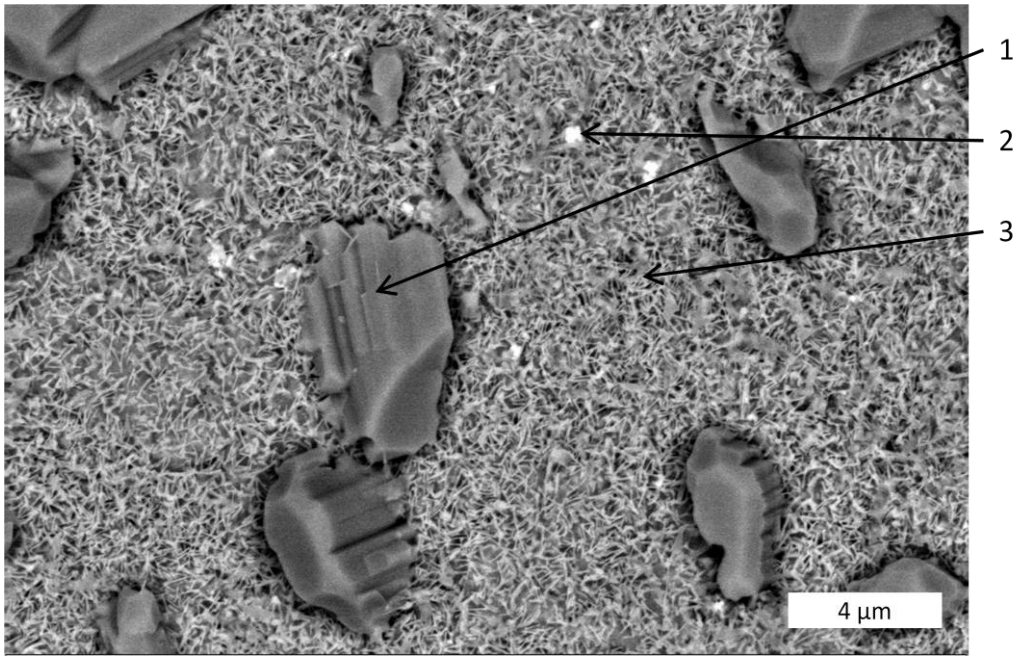

Figure 30. SEM backscattered image of Sanergy HT with 10 nm cerium coating after 500 h exposure in 34% steam and 3% hydrogen at 850°C. The marked spots have been analyzed with EDX and the compositional results are given in Table 3.

An additional difference between Ce coated and uncoated Sanergy HT exposed in fuel side conditions was the presence of large crystallites of up to 7µm on the samples coated with Ce . EDX spot analysis was performed on the three points marked in Figure 30 and the results are presented in Table 3. The large crystals were found to be rich in Mn and Si and the ratio between Mn+Fe to Si was found to be around 2. The lamella shaped oxide crystals had a Cr to Mn ratio matching with that of Cr_2MnO_4 and the crystallites that appeared bright in the image were confirmed to be rich in Ce, even though they were too small to get good quantitative data. The Ce coated Sanergy HT sample was later analyzed with X-ray diffraction and the pattern, is displayed in Figure 31. This XRD pattern matched with two types of oxides: manganese silicate (tephroite) with dissolved iron which had the chemical formula $Mn_{1.4}Fe_{0.6}SiO_4$ and chromium manganese spinel (Cr_2MnO_4). These matches are in good agreement with the results from EDX analysis.

Table 3. Compositional results from EDX analysis at 12kV acceleration voltage. The compositions are given in atomic% and the analysed spots are found in Figure 30.

Spectrum	O	Si	Ti	Cr	Mn	Fe	Ce
1	65.4	11.6	-	0.7	19.2	3.0	-
2	67.2	3.5	0.9	10.7	7.7	5.3	4.8
3	57.6	0.2	0.4	22.8	12.4	6.7	-

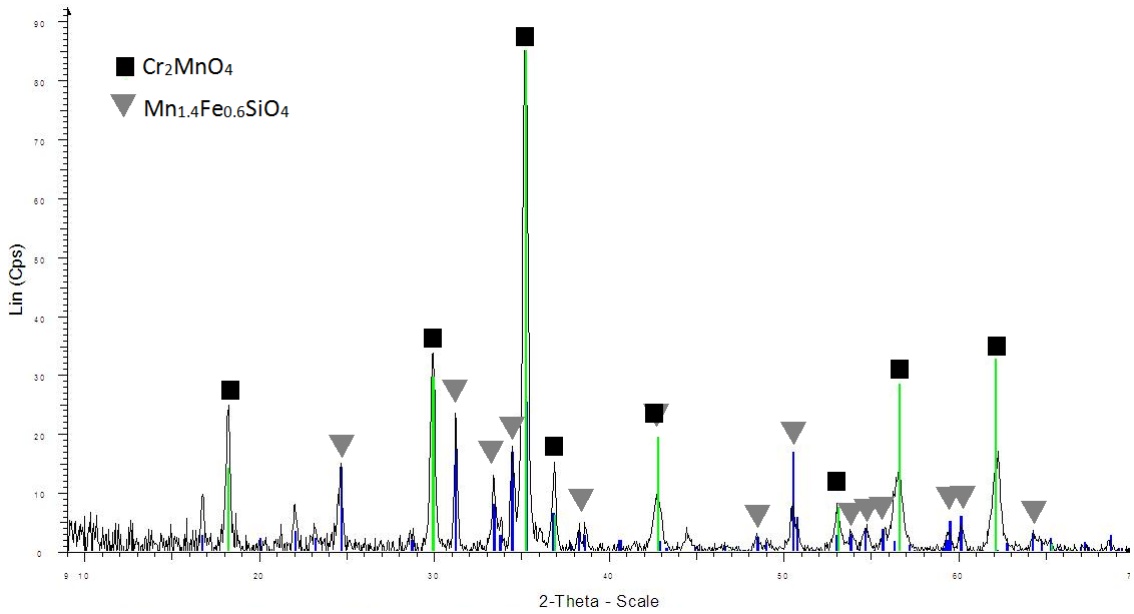

Figure 31. XRD pattern for a sample of Sanergy HT with 10nm cerium coating exposed in 43% steam and 3% hydrogen for 500h at 850°C.

4.3 Chromium-evaporation

Chromium evaporation of Crofer 22H has been measured in 25%, 50% and 100% oxygen and the results are presented in Figure 32. The measurements at 25% and 50% oxygen have been repeated in two different furnaces and all data points are plotted in Figure 32. The data varied by 1% and 5% in 25% and 50% oxygen respectively and are thus difficult to distinguish in the plot. The chromium evaporation seems to have a linear correlation to oxygen pressure in the tested conditions, but it should be noted that the chromium evaporation in 100% oxygen only was tested once. However, the small deviation observed for the exposures in lower pressures makes this assumption credible. A value of $4.7*10^{-5}$kg*m^{-2} evaporated chromium was observed after 168h in 100% oxygen atmosphere. This result can be compared with $4.3*10^{-4}$ kg*m^{-2} evaporated chromium after the same time for Crofer APU, an alloy similar to Corfer 22H, in air with 3% steam [50]. This environment represents the oxygen side of an SOC run in SOFC mode and it can be concluded that the evaporation rate in this atmosphere is almost one magnitude larger compared to in 100% dry oxygen, which represents the oxygen side of a SOC run in SOEC mode without any leakages.

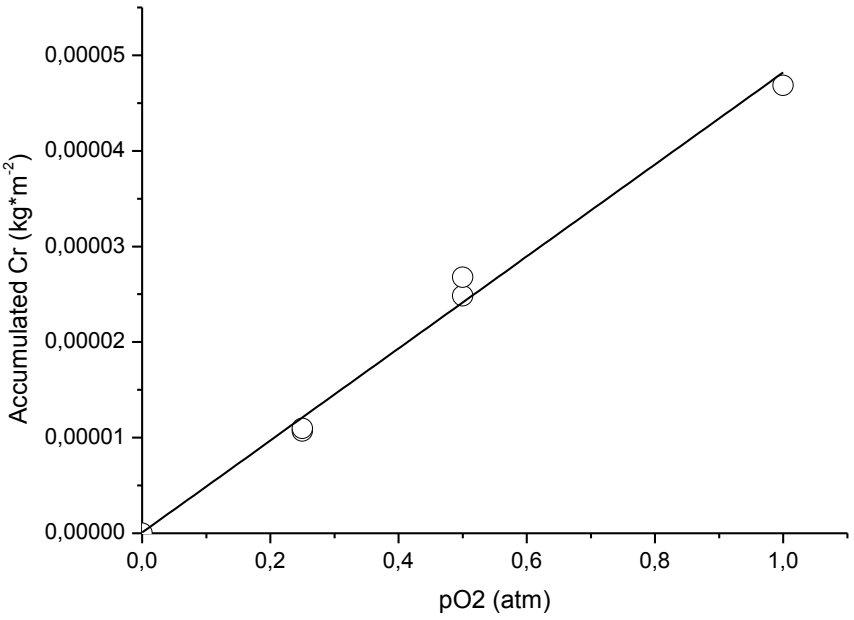

Figure 32. Measured accumulated volatile chromium after 168h from Crofer 22H exposed at 850°C as a function of oxygen partial pressure.

5 Discussion

5.1 AL 441 HP

AL 441 HP, manufactured by ATI metals, is a slightly modified version of the type 441 steel, which is a common commercial high temperature grade ferritic steel [52]. Compared to the other materials tested in this study it is the material with the lowest cost. The composition of this steel also differs from the others (see Table 1) in that it has the lowest amount of chromium. Furthermore, this alloy does not include the creep strengthening elements W or Mo, nor any reactive elements, such as La, Zr or Ce, which reduces manufacturing costs. It does however have similar content of Nb compared to the other materials, which is expected to increase creep strength by Laves phase formation and tie up Si.

In oxygen side exposures AL 441 HP has, together with Crofer 22H, the highest observed oxidation rates (see Figure 21). However, this particular batch of Crofer 22H seemed to have poor corrosion resistance compared to previous batches (see section 5.3). It would seem that the lower amount of Cr and lack of reactive elements results in higher oxidation rate for AL 441 HP. Comparison with the other ATI metals steel E-brite indicates that the low Cr content would be the crucial factor for the increased oxidation rate of AL 441 HP in oxygen side atmosphere. E-brite also lacks any reactive element but has much higher Cr content and looks to have much lower oxidation rate in 100% oxygen. Even if this steel spalled tiny pieces of its oxide scale in this atmosphere it can be assumed to have substantially lower oxidation rate than AL 441 HP in the same environment.

The theory of low Cr content being the cause of the comparably high oxidation rate is further confirmed by the results from fuel side exposures. In this environment the scale of E-brite is well adherent and the oxidation rate low compared to AL 441 HP. The oxidation rate of the latter steel is also significantly increased in fuel side conditions compared to oxygen side conditions. No explanation for this increase could be concluded in terms of alloy composition, but comparison of the surface morphology of the samples exposed in the two environments suggests some explanation. Figure 33 shows a SEM image taken with a secondary electron detector which gives a good representation of the topography of AL 441 HP exposed in fuel side conditions. The porous and assumingly poorly protective structure might be the reason for the accelerated oxidation rate of this steel in steam with hydrogen environment. The surface of the oxide layer formed in oxygen side exposures looks more dense and similar to the other materials in the same environment. It would seem that the oxidation mechanism differ between the two environments. The difference in morphology is also correlated by the difference in oxidation kinetics in fuel and oxygen side conditions. In oxygen environment the parabolic rate law is followed, which indicates that the oxide scale is dense and oxidation rate is controlled by diffusion through this scale. The oxidation rate of AL 441 HP in fuel side exposures is not parabolic, but closer to linear, which indicates a poorly protective oxide scale. Even though AL 441 HP would be a good material in terms of cost, it does not seem to be suitable to be used as interconnect material in SOEC stacks operating under the tested conditions, especially due to the poor corrosion resistance in fuel side conditions.

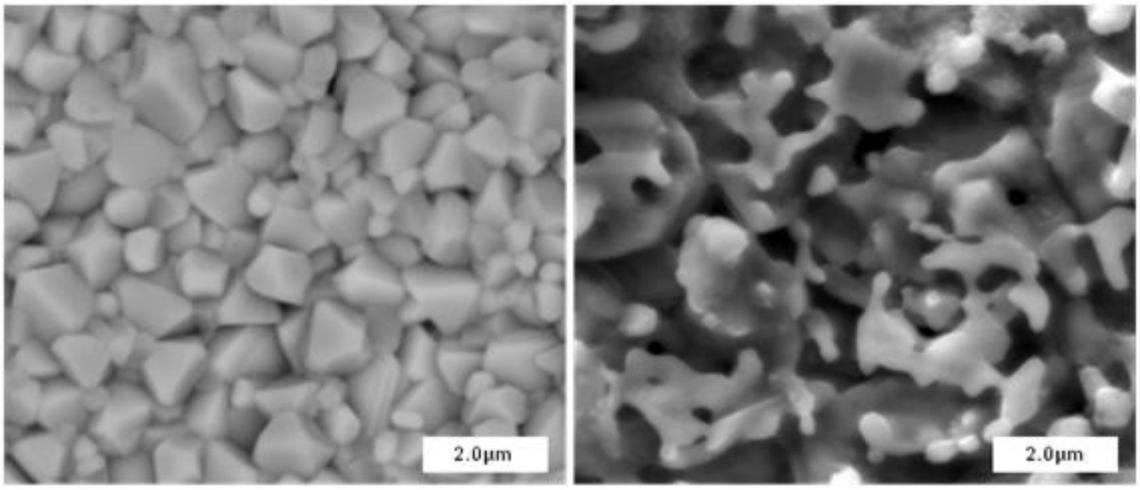

Figure 33. AL 441 HP exposed for 500h at 850°C in pure oxygen (left, BSE image) and 34% steam and 3% hydrogen (right, SE image).

5.2 E-brite

Some discussion about E-brite preceded in the section above. Like AL 441 HP it is manufactured by ATI metals and is commercialized to be used in SOFCs. This ferritic steel is produced through vacuum melting which results in higher purity and lower amounts of Si [53]. The vacuum melting step adds cost to the production compared to AL 441 HP. E-brite is alloyed with the refractory element Mo which is expected to increase creep strength, but like AL 441 HP it does not have any reactive elements which allows for more economic manufacturing. Compared with the other steels E-brite has higher amount of Cr which at intermediate

temperatures increases the risk of forming σ-phases of Cr and Fe which increases brittleness of the alloy [54].

From the mass gain results in 100% oxygen exposure (see Figure 16) E-brite seems to have good corrosion resistance, but SEM analysis revealed minor spallation. Hence, the mass gain data are not accurate, however since the extent of spallation was low the mass gain can be approximated to be proportional to the oxidation rate and it would seem that E-brite has low oxidation rate compared to most of the other materials in this environment. Compared to the other alloys E-brite has lower amount of Nb. Niobium is known to tie up silicon in Laves phases, which means that the lower Nb content in this steel could mean that there is sufficient amount of "free" silicon that can form SiO_2 underneath the chromia layer and cause spallation. Cross-sectional analysis would have to be performed to confirm this. In 1% and 0.01% oxygen atmospheres the spallation was severe and seemed to worsen with decreased oxygen partial pressure. No explanation can be given for this correlation.

In fuel side conditions the oxide scale formed on E-brite samples seemed well adherent and the oxidation rate was low. This increased scale adherence is probably due to the high water content in the experiment atmosphere. An explanation of the increased scale adherence due to the presence of water and hydrogen is provided in a review article by Quadakkers et al.[12]. According to Quadakkers the fuel side environment results in reduced void formation at the metal – oxide interface. With the oxide scale well adherent to the steel, the high Cr content seem to result in low oxidation rates for E-brite. However, the severe spallation in oxygen side conditions makes this alloy poorly suited for SOC applications.

5.3 Crofer 22H

Of the tested materials Crofer 22H, produced by ThyssenKrupp VDM, is the most well known and commonly used ferritic steel in SOC contexts. The alloy contains almost 2wt% of W for increased creep strength and also the reactive element La for improved oxidation resistance and scale adherence [55]. Indeed the adherence of the oxide scale seemed to be good on all tested Crofer 22H samples in both oxygen and fuel side environments. However, the oxidation rate was quite high in oxygen side exposures, but this oxidation rate seems to be related to the specific received batch. Another study at Chalmers University has shown that this specific batch of Crofer 22H has significantly higher oxidation rates in air with 3% steam at 850°C than previously received batches [56]. Even though the received compositional information of this batch seems to be within specifications, other factors such as annealing and surface treatment of the alloy can affect the oxidation behavior.

The oxidation rate of Crofer 22H in fuel side conditions was significantly lower than in oxygen atmospheres and comparable with Sanergy HT which has similar alloy composition. This indicates different oxidation mechanism in the two environments. If this effect is correlated to this specific batch or is a general material feature remains to be investigated. The surface morphology of the Crofer 22H samples looked similar to all the other materials exposed in oxygen side atmospheres (see Figure 29) and had whisker or lamella shaped structure after fuel side exposure (see Figure 27), which is the structure often found on chromia forming alloys in fuel side conditions [12]. The oxidation rate in fuel side environment does seem to fit well with the parabolic rate law, but it can be argued that it deviates slightly in oxygen side conditions, which would further confirm a theory of different mechanisms in the two environments.

5.4 Sanergy HT

Sanergy HT is an alloy produced by Sandvik Materials Technology and is specifically designed for SOC interconnects [57]. Its composition is very similar to Crofer 22H with the difference of having the refractory element Mo instead of W and the reactive element Zr instead of La. The oxide scale of Sanergy HT samples seemed well adherent in all exposures and the amount oxidation was in the lower range relative to other materials. Furthermore, no major difference in mass gain between fuel and oxygen side exposures was observed. However, the oxidation kinetics was not the same in oxygen and fuel side environments (Figure 23-26). Oxidation rates of Sanergy HT samples exposed in dry oxygen follow the parabolic rate law but this is clearly not the case in steam with hydrogen. In fuel side conditions the oxidation rate looks more logarithmic than parabolic as can be seen in Figure 34. The same change in oxidation behavior was not observed for the samples coated with 10nm Ce (see Figure 26), although it can be argued that oxidation rate deviates slightly from parabolic oxidation rate in fuel side environment. This indicates that cerium does not only reduce the oxidation rate, but also alters the oxidation mechanism of the steel, at least in fuel side conditions.

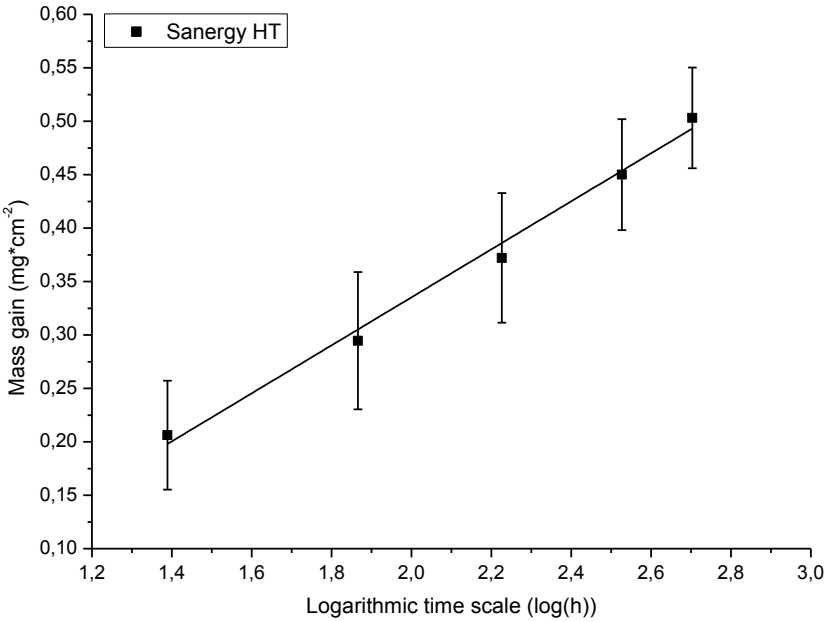

Figure 34. Average mass gain of Sanergy HT exposed in 34% steam and 3% hydrogen plotted against the logarithm of the exposure time.

Another difference between uncoated and coated Sanergy HT samples was the surface morphology after exposure in fuel side conditions (see Figure 29 and Figure 30). The top layer of uncoated samples did not consist of whisker or lamella shaped oxide, whereas the surface of Ce coated samples did. This further implies that the oxidation mechanism is altered when cerium is present but contradicts observations found in the literature. Quadakkers et al. states that formation of whisker type oxides are the result of predominant Cr diffusion and consequent outwards growth of the oxide scale and reports that “optimum” additions of reactive elements added through oxide dispersion in chromium based alloys reduces the tendency of whisker formation [12]. This decreased extent of whisker formation is attributed to the RE effect of suppressing outward growth. Indeed the presence of reactive elements in chromia forming alloys has been shown to change the oxidation mechanism from predominant Cr outward

diffusion to O inward diffusion [48]. The fact that whiskers were found on Ce coated samples, but not on uncoated samples, could indicate interesting effects that are worthwhile to study in more detail.

In fuel side conditions the Ce coating on Sanergy HT samples also seemed to promote the formation of large manganese silicate crystals on the surface as can be seen in Figure 35 and with larger magnification in Figure 30. The XRD pattern of an analyzed sample matched with $Mn_{1.4}Fe_{0.6}SiO_4$ (see Figure 31) from the database. Compositional information from EDX analysis (see Table 3) fits better with manganese silicate with slightly higher Mn content, i.e. $Mn_{1.7}Fe_{0.3}SiO_4$, which should have almost the same crystal cell parameters since the atomic radii of Mn and Fe are very similar. Whichever the ratio of Fe and Mn is, the fact still remains that large amounts of silicates are present on the surface of an alloy with minor content of Si. This raises suspicions of external contaminants on the samples, but it should be noted that these silicates were not observed on any of the other materials, nor on the uncoated Sanergy HT samples. Furthermore, the same observation has been made on two samples from two replicated exposures in fuel side conditions and no silicates were found on unexposed samples. The reaction chamber and sample holder used in the exposures were made of alumina, so it is unlikely that the samples were contaminated during exposures. Calculations (see (24)) that includes the density of pure Mn_2SiO_4 (tephroite) and the Si content in the received batch of Sanergy HT results in a continuous tephroite layer with a theoretical maximum thickness of 1,7µm, which seems plausible if one looks at Figure 35. This suggests that the tephroite on the surface of these samples could indeed be the result of reaction with Si from the alloy.

$$d = \frac{n_{Si} * M_{\mathrm{Mn2SiO4}}}{A * \rho_{\mathrm{Mn2SiO4}}} \tag{24}$$

Where d is the thickness of the tephroite layer, $M_{Mn2SiO4}$ the molar mass of tephroite, n_{Si} the molar amount of Si in a sample, A the sample area and $\rho_{Mn2SiO4}$ the density of tephroite.

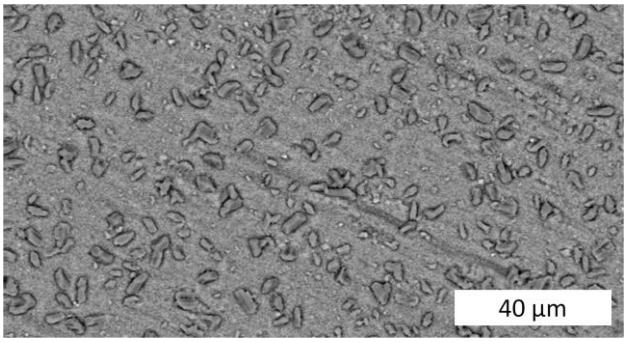

Figure 35. SEM backscattered image of a Sanergy HT with 10nm Ce coating exposed in 34% steam and 3% hydrogen.

The conditions in the fuel side exposures in this study corresponds to an oxygen partial pressure in the order of 10^{-14} and the data from Figure 36 confirms that Mn_2SiO_4 is thermodynamically stable under these conditions. Higher oxygen partial pressures would result in the formation of $MnSiO_3$. Thermodynamic calculations for the reaction of $MnCr_2O_4$ with SiO_2 under fuel side conditions have been performed with the software Factsage. When calculations with spinel data from ternary Mn-Cr-O systems were performed silica was stable, but when this data was

excluded the result was the formation of tephroite and chromia according to the following equation

$$2\,\mathrm{MnCr_2O_4(s)} + \mathrm{SiO_2(s)} = Mn_2\mathrm{SiO_4(s)} + Cr_2\mathrm{O_3(s)} \qquad (25)$$

It could be argued that the data for the ternary Mn-Cr-O system did not include Si and is therefore not correct. From these calculations it seems that tephroite formation could be plausible. Together with mass balance calculations on the silica content in the steel it would seem that these manganese silicates are not the result of contamination from an external source.

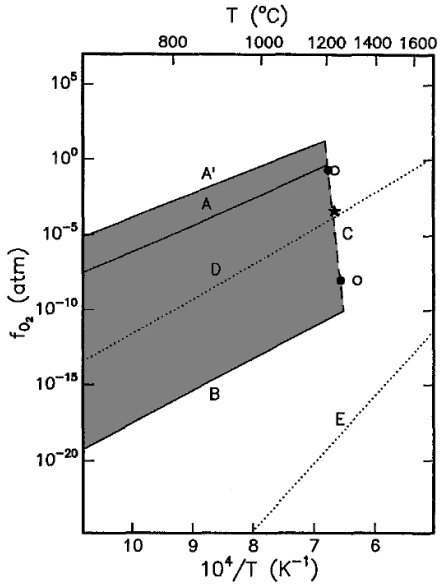

Figure 36. Stability diagram of Mn_2SiO_4 in different oxygen partial pressures and temperatures. The gray field represents the conditions where Mn_2SiO_4 is thermodynamically stable. Modified figure from Ref. [58].

An estimation by using conductivity data from studies on Mn_2SiO_4 by Bai et al. and on Cr_2O_3 by Ku and Winterbottom is that the conductivity of Cr_2O_3 is at least one order of magnitude higher than for Mn_2SiO_4 [58][59]. This should mean that the formation of manganese silicates on the steel surface reduces conductivity through the material and would lead to higher electrical losses in a SOC. However, to make such a conclusion area specific resistance (ASR) measurements of the sample would be needed.

5.5 Oxygen pressure dependence

5.5.1 Oxidation

Results from exposures in dry atmosphere with different oxygen partial pressures (see Figure 21) do not indicate a trend between oxidation rate and oxygen partial pressure in the investigated pressure range. In Figure 37 the mass gain data from the chromium evaporation experiments and gravimetric experiments after 168h have been combined. A peak in oxidation rate is observed for the 1% oxygen atmosphere, but the shorter exposure time in this case makes it less pronounced than what is observed after 500h in Figure 21. No trend of change in oxidation rate as function of oxygen partial pressure could be concluded from either of the figures. The surface kinetics of the oxidation process should be independent of oxygen pressure,

at least for the materials that had parabolic oxidation rate since this indicates that diffusion through the oxide scale is the rate limiting step. However, bulk diffusion rate of Cr in chromia crystals is a function of oxygen partial pressure and consequently the oxidation rate should also be dependent on oxygen concentration. Nevertheless, other studies have also concluded that oxidation rate is independent of oxygen partial pressure in the studied temperature range and oxygen partial pressures [60]. This could be due to the fact the scale growth is predominantly governed by diffusion through the grain boundaries which are expected to have different defect structure and oxygen pressure dependence than the chromia crystals.

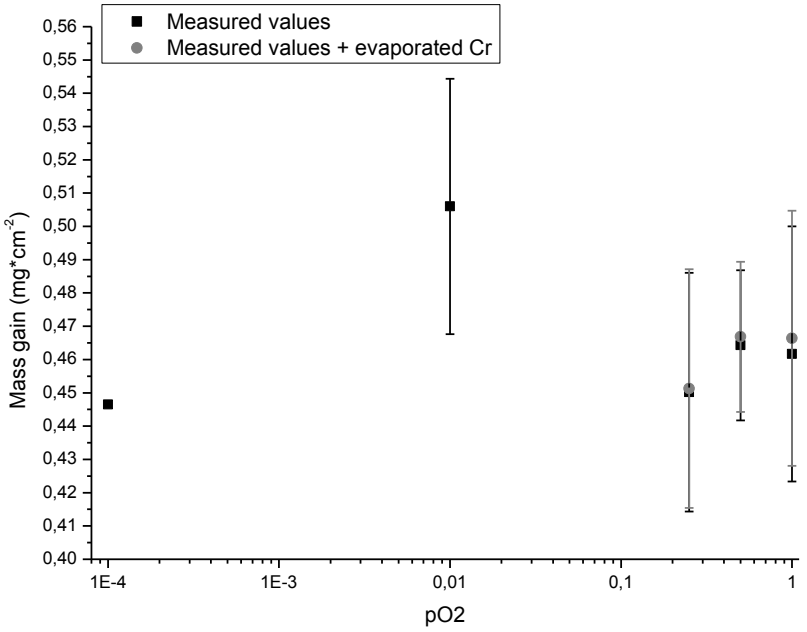

Figure 37. Mass gain for Crofer 22H exposed for 168h at 850°C as a function of oxygen partial pressure. The data is put to together from chromium evaporation and gravimetric experiments. The gray data points represent the mass gain with the mass of evaporated Cr added.

Additionally, a difference in size of the surface crystallites formed in 100% and 1% oxygen was detected for all materials (see Figure 27) and the crystallites were always smaller in 1% oxygen. The finer grain structure formed in this atmosphere is expected to lead a higher rate of Cr transport through the grain boundaries which could be the reason for the slightly accelerated oxidation in 1% oxygen. An explanation to why the oxidation rate decreases again in 0.01% could not be provided and the samples exposed in 0.0.1% remains to be analyzed.

5.5.2 Chromium evaporation

Chromium evaporation of Crofer 22H showed a linear correlation with oxygen partial pressure in the investigated environment. This differs slightly from what would be expected from the thermodynamics of the reaction of chromia and oxygen to form CrO_3 (16). If equilibrium is assumed the evaporation rate should be proportional to $p(O_2)^{¾}$ according to the following equation

$$p(CrO_3) = k * a(Cr_2O_3) * p(O_2)^{¾} \quad (26)$$

Where p*n* denotes the respective partial pressures, aCr_2O_3 the activity of chromia and k the equilibrium constant. In this case aCr_2O_3 can be counted as unity (since it is a solid). The

deviation from this correlation indicates the reaction was not in equilibrium i.e. the gas flow speed was too high for equilibrium to be reached. When the chromium evaporation is governed by reaction kinetics the correlation above does not apply and the rate could have another correlation to oxygen partial pressure.

As was discussed in section 2.5 chromium evaporation in dry oxygen atmosphere is significantly lower than in steam containing oxygen atmosphere. This raises the question of whether the dryness of the experimental setup is sufficient to neglect evaporated chromium by reaction with trace amounts of water. The gases used during the experiments were specified with 99.999% purity. This leaves the possibility of 10 ppm of water impurities plus additional leakage from atmosphere through tubes and couplings. The thermochemistry of the reactions to form volatile chromium species have been studied in Refs. [26] and [27] and data from these studies has been used to construct Figure 38. From this graph it can be concluded the predominant formed volatile chromium species should be CrO_3.

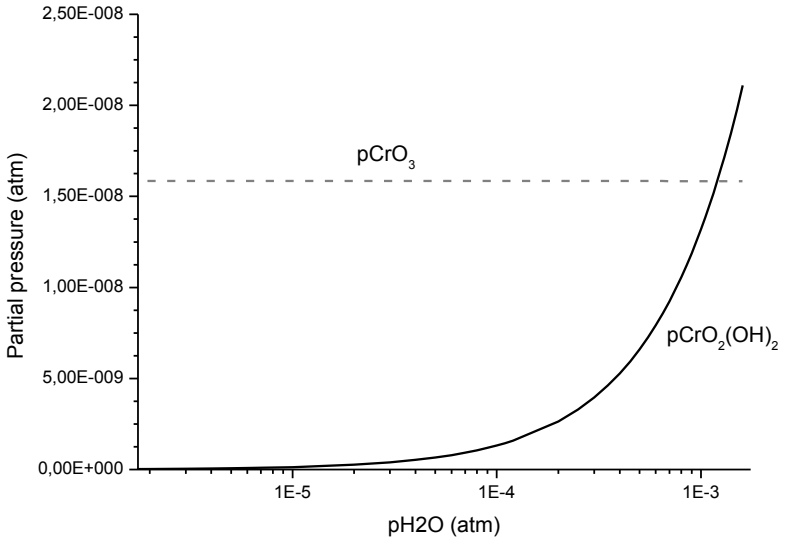

Figure 38. Partial pressures of CrO_3 and $CrO_2(OH)_2$ as a function of water partial pressure at 850°C and 1 atm oxygen pressure. Based on thermodynamic data from Refs. [26] and [27].

From the amount of collected chromium the partial pressure of CrO_3 was calculated to be approximately one fifth of the theoretical value. This can be explained partly by that the evaporation reaction does not seem to reach equilibrium in the tested conditions, but more importantly the top layer oxide should consist of $MnCr_2O_4$ which has lower activity than Cr_2O_3. In other words the added Mn in the alloy is working as intended to reduce chromium evaporation. The question if this reduction is sufficient from a SOEC stack point of view remains to be examined. If the linear trend of chromium evaporation as a function of oxygen pressure is indeed continued at higher pressures the evaporation rate will be significantly increased. Additionally this study was conducted under extremely dry conditions which would represent a cell stack with no leakage. From Figure 38 it can be seen that water contents as low as 0.1% could lead double the amount of chromium evaporation. This is also crucial for life

time estimations of interconnects since the rate chromium loss from the steel is increased, which will be discussed further in the following section.

5.6 Estimated steel life time

The agreement of the parabolic rate law for many of the tested materials suggests that the oxidation kinetics is diffusion controlled in most cases. This allows for calculation of the chromium loss in the steel as a function of exposure time

$$\Delta m_{Cr} = \frac{2M_{Cr}}{3M_O}\sqrt{k_p t} \qquad (27)$$

Where k_p is the parabolic rate constant, Δm_{Cr} the mass loss of chromium, t the time and M_{Cr} and M_O the molar masses of Cr and O respectively. Parabolic rate constants for the respective materials can been retrieved in Table 2. This equation gives an estimation of the chromium loss, granted that the oxidation mechanism and rate remains the same during the extrapolated time interval. Additionally the linear correlation of chromium evaporation with oxygen pressure makes it possible to calculate the evaporation rate at different oxygen partial pressures for Crofer 22H. In Figure 39 the parabolic rate constant for Crofer 22H in 100% oxygen and the evaporation rate from Figure 32 have been used to plot Cr loss of a 0.2mm thick sample with an initial Cr content of 22wt% as a function of time. In this case the critical Cr content was chosen to 15wt% since there is high chance that a chromia scale cannot form at this level, which would lead to break away corrosion. Extrapolations of the chromium evaporation rate data have been performed up to estimate the evaporation up to 50bar. The validity of this approach can be questioned since extrapolations far outside of the investigated oxygen pressure range have been performed. This has been done to give a rough estimation of the impact of oxygen pressure on interconnect lifetime. Figure 32 shows that when the operating pressure is increased chromium evaporation becomes a crucial factor for interconnect and stack lifetime. It can also be concluded that the measured oxidation rate of Crofer 22H in this study is too high for the material to be used in SOEC stacks, which should operate for 40 000h or more, but it should be noted that the tested batch seems to have less corrosion resistance than previously tested batches at this laboratory.

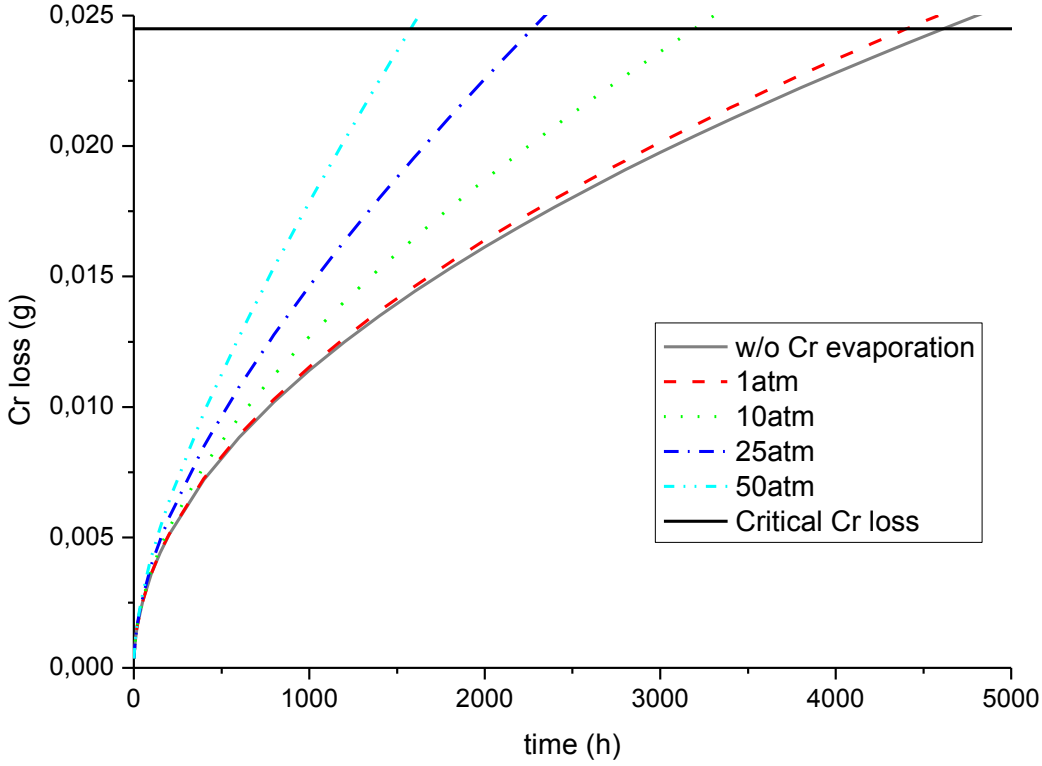

Figure 39. Calculated loss of chromium as a function of time for Crofer 22H in different oxygen pressures under the conditions used in this study, i.e. 850°C and 3.8cm/s gas flow rate.

6 Conclusions

The present work showed that the degradation behavior of the investigated steels varied substantially although the compositions were relatively similar. Most of the investigated materials showed parabolic oxidation rate in the tested atmospheres which indicates that oxidation rate is limited by solid state diffusion. A few materials deviated from parabolic oxidation, especially so in fuel side conditions. Exposure to fuel side environment seemed to change the oxidation mechanisms for some materials compared to oxygen environments.

One material that exhibited low corrosion rates in all investigated environments was Sanergy HT. A Ce coated version of the same material performed even better, however the formation of $(Mn,Fe)_2SiO_4$ was observed in fuel side conditions, which might be detrimental. E-brite suffered from extensive spallation in dry oxygen atmospheres, which makes this material less suitable to be used for interconnects in SOEC applications. The suitability of AL 441 HP in SOECs is also questionable due to the poor corrosion performance and spallation in fuel side conditions.

Small variations in oxidation rate were observed in different partial pressures of dry oxygen, however no apparent correlation could be observed. It is suggested that the oxidation rate can be approximated as independent of oxygen partial pressure within the investigated pressure range. The adhesion of the oxide scale of E-brite was strongly affected by the oxygen partial pressure in the dry atmospheres. Chromium evaporation had a linear correlation to oxygen pressure in the investigated pressure range. This means that chromium evaporation is expected to be of more concern when operating SOECs under high pressures.

Chromium evaporation in dry O_2 at atmospheric pressure is substantially lower than in a typical SOFC oxygen side environment (3% H_2O) and not expected to have a major impact on interconnect lifetime. However, the presence of H_2O on the oxygen side of a SOEC, e.g. due to leakage, as well as operation under elevated pressure is expected to accelerate Cr evaporation significantly and would thus make Cr evaporation a major lifetime limiting factor.

6.1 Restrictions

In an actual cell stack the interconnect is exposed to fuel gases on one side and oxygen on the other. Some reports indicate that this dual atmosphere can result in slightly different oxidation mechanisms of the interconnect steel than in single atmosphere exposure [61][62]. Additionally the interconnects inherently have applied potential and consequently current flowing through them, which theoretically should affect the oxidation [22]. Neither dual atmosphere nor applied current experiments have been performed due to limitations both with apparatus and the time scale of a master's thesis.

6.2 Suggestions for future work

Cross sectional analysis of the oxide scales with SEM and EDX would hopefully help in trying to find out the reasons for some of the changes in oxidation behavior seen on some samples between different exposure environments. Additional testing of chromium evaporation and oxidation rate in high and low oxygen partial pressure respectively is recommended to get more statistics which would increase credibility in extrapolation of the suggested correlations to higher oxygen pressures. The next step of this study could be to build systems where exposures at a few bar pressure could be performed safely. To further investigate the oxygen dependence and reaction kinetics of chromium evaporation studies with varied flow rates could be performed.

7 References

[1] M. Balat, "Possible methods for hydrogen production," *Energy Sources,* vol. 30:1, no. Part A: Recovery, Utilization, and Environmental Effects, pp. 39-50, 2009.

[2] M. Laguna-Bercero, "Recent advances in high temperature electrolysis using solid oxide fuel cells: A review," *Journal of Power Sources,* vol. 203, pp. 4-16, 2012.

[3] Y. Bo et al., "Advance in highly efficient hydrogen production by high temperature steam electrolysis," *Science in China Series B: Chemistry,* vol. 51, no. 4, pp. 289-304, 2008.

[4] S. D. Ebbesen and M. Mogensen, "Electrolysis of carbon dioxide in Solid Oxide Electrolysis Cells," *Journal of Power Sources,* vol. 193, no. 1, pp. 349-358, 2009.

[5] S. H. Jensen, X. Sun, S. D. Ebbesen and R. Knibbe, "Hydrogen and synthetic fuel production using pressurized oxide electrolyis cells," *International journal of hydrogen energy,* vol. 35, no. 18, p. 9544–9549, 2010.

[6] C. Stoots, J. O'brien and J. Hartvigsen, "Results Of Recent High Temperature Co-Electrolysis Studies At The Idaho National Laboratory," *International Journal of Hydrogen Energy,* vol. 34, no. 9, p. 4208–4215, 2009.

[7] N. J. Maskalick, "High Temperature Electrolysis Cell Performance," *International Journal of Hydrogen Energy,* vol. 11, no. 9, p. 563–570, 1986.

[8] G. Schiller, A. Ansar, M. Lang and O. Patz, "High temperature water electrolysis using metal supported solid oxide electrolyser cells (SOEC)," *Journal of Applied Electrochemistry,* vol. 39, no. 2, pp. 293-301, 2009.

[9] F. Lefebvre-Joud, A. Brisse, J. Bowen and P. Ouweltjes, "Durability and Effciency of High Temperature Steam Electrolysis as Studied in the RelHy Project," in *WHEC*, Essen, Germany, 2010.

[10] J. S. Herring, J. E. O'Brien, C. M. Stoots, G. Hawkes, J. J. Hartvigsen and M. Shahnam, "Progress in high-temperature electrolysis for hydrogen production using planar SOFC technology," *International Journal of Hydrogen Energy,* vol. 32, no. 4, p. 440–450, 2007.

[11] J. A. Turner, "Sustainable hydrogen production," *Science,* vol. 305, no. 5686, pp. 972-974, 2004.

[12] W. Quadakkers, J. Piron-Abellan, V. Shemet and L. Singheiser, "Metallic interconnectors for solid oxide fuel cells - a review," *Materials at High Temperatures,* vol. 20, no. 2, pp. 115-127, 2003.

[13] P. Atkins and L. Jones, "Electrochemistry," in *Chemical Principles The Quest for Insight*, New York, W. H. Freeman and Company, 2008, pp. 483-528.

[14] J. McMurry and R. C. Fay, "Electrochemistry," in *Chemistry*, New Jersey, Prentice Hall, 2001, pp. 759-810.

[15] [Online]. Available: http://upload.wikimedia.org/wikipedia/commons/3/37/Hofmann_voltameter_fr.svg.

[16] P. Atkins, J. de Paula and R. Friedman, "Chemical Equilibrium," in *Quanta, Matter and Change: A molecular approach to physical chemistry*, Oxford, Oxford University Press, 2009, pp. 558-587.

[17] M. Shen, N. Bennett, D. Yulong and K. Scott, "A concise model for evaluating water electrolysis," *International Journal of Hydrogen Energy,* vol. 36, no. 22, pp. 14335-14341, 2010.

[18] M. Ni, M. K. Leung and D. Y. Leung, "Technological development of hydrogen production by solid oxide electrolyzer cell (SOEC)," *International Journal of Hydrogen Energy,* vol. 33, no. 9, p. 2337 – 2354, 2008.

[19] K. K. Subhash C. Singhal, High Temperature Solid Oxide Fuel Cells: Fundamentals, Design and Applications, Amsterdam, The Netherlands: Elsevier, 2003.

[20] A. D. James Larminie, Fuel Cell Systems Exlpained, Chichester, England: John Wiley & Sons Ltd., 2003.

[21] N. Birks, G. H. Meier and F. S. Pettit, Introduction to the High Temperature Oxidation of Metals, 2nd ed., Cambridge: Cambridge University Press, 2006, pp. 144-149.

[22] P. Kofstad, High temperature corrosion, Barking, England: Elsivier Applied Science Publishers Ltd., 1988.

[23] L. E. Smart and E. A. Moore, Solid State Chemistry: An Introduction, 3rd ed., Boca Raton: CRC Press, 2005.

[24] N. Pilling and R. Bedworth, "The Oxidation of Metals at High Temperatures," *Journal Institute of Metals,* vol. 29, pp. 529-591, 1923.

[25] J. Froitzheim, "Ferritic Steel Interconnectors and heir Interactions with Ni Base Anodes in Solid Oxide Fuel Cells (SOFC)," RWTH Aachen, Jülich, 2008.

[26] E. J. Opila, D. L. Myers, N. S. Jacobson, I. B. Nielsen, D. F. Johnson, J. K. Olminsky and M. D. Allendorg, "Theoretical and Experimental Investigation of the Thermochemistry of CrO2(OH)2(g)," *The Journal of Physical Chemistry A,* vol. 111, no. 10, p. 1971–1980, 2007.

[27] B. B. Ebbinghaus, "Thermodynamics of gas phase chromium species: The chromium oxides, the chromium oxyhydroxides, and volatility calculations in waste incineration processes," *Combustion and Flame,* vol. 93, no. 1-2, pp. 119-137, 1993.

[28] W. Zhu and S. Deevi, "Development of interconnect materials for solid oxide fuel cells," *Materials Science and Engineering: A,* vol. 348, no. 1-2, pp. 227-243, 2003.

[29] W. Zhu and S. Deevi, "Opportunity of metallic interconnects for solid oxide fuel cells: a status on contact resistance," *Materials Research Bulletin,* vol. 38, no. 6, pp. 957-972, 2003.

[30] B. Church, T. Sanders, R. Speyer and J. Cochran, "Thermal expansion matching and oxidation resistance of Fe–Ni–Cr interconnect alloys," *Materials Science and Engineering: A,* Vols. 452-453, pp. 334-340, 2007.

[31] J. W. Fergus, "Metallic interconnects for solid oxide fuel cells," *Materials Science and Engineering: A,* vol. 397, no. 1-2, pp. 271-283, 2005.

[32] L. Niewolak, E. Wessel, L. Singheiser and W. Quadakkers, "Potential suitability of ferritic and austenitic steels as interconnect materials for solid oxide fuel cells operating at 600

°C," *Journal of Power Sources,* vol. 195, no. 22, pp. 7600-7608, 2010.

[33] J. Wu and X. Liu, "Recent Developement of SOFC Interconnect," *Journal of Material Science Technology,* vol. 26, no. 4, pp. 293-305, 2010.

[34] G. Y. Lau et al., "Chromium transport by solid state diffusion on solid oxide fuel cell cathode," *Journal of Power Sources,* vol. 195, no. 22, pp. 7540-7547, 2010.

[35] T. Horita et al., "Chromium Poisoning and Degradation at (La, Sr)MnO3 and (La,Sr)FeO3 Cathodes for Solid Oxide Fuel Cells," *Journal of The Electrochemical Society,* vol. 157, pp. B614-B620, 2010.

[36] J. Froitzheim and J. Svensson, "Nanocoatings for SOFC interconnects - Mitigating chromium volatilization and improving corrosion properties," *Materials Science Forum,* vol. 696, pp. 412-416, 2011.

[37] P. Huczowski and W. Quadakkers, "Effect of geometry and composition of Cr steels on oxide scale properties relevant for interconnector applications in Solid Oxide Fuel Cells (SOFCs)," Research Center Jülich, Energy Technology 65, Jülich, 2007.

[38] C. Johnsson et al., "The effect of coating crystallization and substrate impurities on magnetron sputtered doped LaCrO3 coatings for metallic solid oxide fuel cell interconnects," *International Journal of Hydrogen Energy,* vol. 34, no. 5, pp. 2408-2415, 2009.

[39] K. Yamamoto, Y. Kimura, F.-G. Wei and Y. Mishima, "Design of Laves phase strengthened ferritic heat resisting steels in the Fe–Cr–Nb(–Ni) system," *Materials Science and Engineering,* Vols. 329-331, p. 249–254, 2002.

[40] N. Nabiran, S. Weber and W. Theisen, "Influence of Intermetallic Precipitates and Heat Treatment on the Mechanical Properties of High-Temperature Corrosion Resistant Ferritic Steels," *Procedia Engineering,* vol. 10, pp. 1651-1656, 2011.

[41] J. Froitzheim, G. Meier, L. Niewolak, P. Ennis, H. Hattendorf, L. Singheiser and W. Quadakkers, "Development of high strength ferritic steel for interconnect application in SOFCs," *Journal of Power Sources,* vol. 178, no. 1, pp. 163-173, 2008.

[42] Z. Yang, G.-G. Xia, C.-M. Wang, Z. Nie, J. Templeton, J. W. Stevenson and P. Singh, "Investigation of iron–chromium–niobium–titanium ferritic stainless steel for solid oxide fuel cell interconnect applications," *Journal of Power Sources,* vol. 183, no. 2, p. 660–667, 2008.

[43] A. Holt and P. Kofstad, "Electrical conductivity Cr2O3 doped with TiO2," *Solid State Ionics,* vol. 117, no. 7-8, pp. 21-25, 1999.

[44] F. Pirón Abellán and W. Quadakkers, "Developement of Ferritic Steels for Applications as Interconnect Materials for Intermediate Temperature Solid Oxide Fuel Cells (SOFCs),"

Forschungszentrums Jülich, Jülich, 2005.

[45] M. Stanislowski, J. Froitzheim, L. Niewolak, W. Quadakkers, K. Hilpert, T. Markus and L. Singheiser, "Reduction of chromium vaporization from SOFC interconnectors by highly effective coatings," *Journal of Power Sources,* vol. 164, no. 2, pp. 578-589, 2007.

[46] Z. Lu and J. Zhu, "Electrical Conductivity of the Manganese Chromite Spinel Solid Solution," *Journal of the American Ceramic Society,* vol. 88, no. 4, pp. 1050-1053, 2005.

[47] P. Y. Hou, "The Reactive Element Effect - Past, Present and Future," *Materials Science Forum,* vol. 696, pp. 39-44, 2011.

[48] P. Hou, I. Browna and J. Stringerb, "Study of the effect of reactive-element addition by implanting metal ions in a preformed oxide layer," *Nuclear Instruments and Methods in Physics Research Section B: Beam Interactions with Materials and Atoms,* Vols. 59-60, no. 2, pp. 1345-1349, 1991.

[49] M. S. Sohal et al., "Critical Causes of Degradation in Integrated Laboratory Scale Cells During High Temperature Electrolysis," U.S. Department of Energy, 2009.

[50] J. Froitzheim, H. Ravash, E. Larsson, J. E. Svensson and L. G. Johansson, " Investigation of Chromium Volatilization from FeCr Interconnects by a Denuder Technique," *Journal of the Electrochemical Society,* vol. 157, no. 9, pp. B1295-B1300, 2010.

[51] M.-C. Fournier-Salaün and P. Salaün, "Quantitative determination of hexavalent chromium in aqueous solutions by UV-Vis spectrophotometer," *Central European Journal of Chemistry,* vol. 5, no. 4, pp. 1084-1093, 2007.

[52] ATI Metals, [Online]. Available: http://www.atimetals.com/Documents/ati_e-brite_tds_en.pdf. [Accessed May 2012].

[53] ATI Metals, [Online]. Available: http://www.atimetals.com/Documents/ati_441_tds_en.pdf. [Accessed May 2012].

[54] J. e. a. Hammer, "The Oxidation of Ferritic Stainless Steels in Simulated Solid-Oxide Fuel-Cell Atmospheres," *Oxidation of Metals,* vol. 67, no. 1, pp. 1-38, 2006.

[55] ThyssenKrupp, [Online]. Available: www.thyssenkrupp.com. [Accessed 24 10 2012].

[56] R. Sachitanad, *Unpublished results,* Chalmers University of Technology.

[57] Sandvik Materials Technology, [Online]. Available: http://www.smt.sandvik.com. [Accessed 24 10 2012].

[58] Q. Bai, Z.-C. Wang and K. D.L., "Manganese Olivine I: Electrical conductivity," *Physics and Chemistry of Minerals,* vol. 22, pp. 489-503, 1995.

[59] R. C. Ku and W. L. Winterbottom, "Electrical Conductivity in Sputter Deposited Chromium Oxide Coatings," *Electronics and Optics,* vol. 127, pp. 241-256, 1985.

[60] E. A. Polman, T. Fransent and P. J. Gellings, "The reactive element effect; ionic processes of grain-boundary segregation and diffusion in chromium oxide scales," *Journal of Physics: Condensed Matter,* vol. 1, pp. 4497-4510, 1989.

[61] Z. G. Yang, G. Xia and J. Stevenson, "Advanced SOFC Interconnect Development at PNNL," *ECS Transactions,* vol. 5, no. 1, pp. 347-356, 2007.

[62] A. W. B. Skilbred and R. Haugsrud, "The effect of dual atmosphere conditions on the corrosion of Sandvik Sanergy HT," *Internation Journal of Hydrogen Energy,* vol. 37, no. 9, p. 8095–8101, 2012.

[63] [Online]. Available: http://upload.wikimedia.org/wikipedia/commons/3/37/Hofmann_voltameter_fr.svg. [Accessed February 2012].